A study on the stability of a high speed compressor

by

Bruno A. Posokhow

MEng. Aeronautical and Astronautical Engineering, Ecole Centrale Paris (1998)

Submitted to the Department of Aeronautics and Astronautics in partial fulfillment of the requirements for the

degree of

Master of Science

at the

Massachusetts Institute of Technology

February 2000

Author_____
Department of Aeronautics and Astronautics
February 2000

Certified by_____
Dr. Choon S. Tan
Senior Research Engineer, Dept. of Aeronautics and Astronautics
Thesis Supervisor

Accepted by_____
Nesbitt W. Hagood
Associate Professor of Aeronautics and Astronautics
Chairman, Department Graduate Committee

A study on the stability of a high speed compressor

by

Bruno André Posokhow

Submitted to the Department of Aeronautics and Astronautics on January 14th, 2000
in partial fulfillment of the requirements for the degree of
Master of Science

Abstract

The competition in the aircraft engine industry has led to the design of highly loaded components while reducing manufacturing costs and fuel consumption. One way to achieve those goals is to raise the pressure ratio across each stage of the engine's compressor by reducing the stability margin that keeps the rotor blades from stalling. To avoid this, it is important to understand how the compressor goes into stall or surge and what is the effect of design changes on compressor performance.

A study on the stability of a two-stage high-speed compressor has been implemented. The original goal was first to determine which one of the two stages is the most unstable and then to determine if the rotor tip leakage flow of the most unstable stage was responsible for setting the compressor stability. This is then to be followed by a delineation of proposed design changes that can potentialy enhance the stability behavior of the 2-stage compressor. The approach essentialy involved applying time-accurate 2-D as well as 3-D CFD codes developed by Hoying and the three-dimensional compressor model which consists of a row-by-row body force representation of a multi-stage compressor developed by Gong. During the course of the study, the CFD codes developed by Hoying has been appropriately modified so that it can be used for the present compressor configuration with variable annulus. The CFD code was used to compute the flow in each individual blade-row for use in formulating the row-by-row body force representation of the two-stage high-speed compressor. It was found that the first stage was the most unstable. An eleven blade passage calculation of the flow in the rotor of the first stage was initiated with the objective of determining if it was the rotor tip leakage flow that set the stability limit of the compressor. This consisted of determining the pressure rise characteristics of the rotor in isolation based on a single blade passage calculation. This is followed by initiating the calculation of the flow field in a 11-blade passage grid for a set of throttle openings in the neighborhood of the throttle setting at stall. The lack of additional computational resources needed for the completion of the required multi-blade passage calculations constrained us to limit the scope of the work reflected in the original stated goal.

Thesis Supervisor: Dr. Choon S. Tan
Title: Senior Research Engineer, Dept. of Aeronautics and Astronautics

ACKNOWLEDGMENTS

I am glad to be able to express my gratitude to those who helped me during the completion of this research and to those who made it possible. In particular, I would like to thank the following persons and organizations.

First, I would like to show my appreciation to the Compressor Aerodynamic department of the research division of SNECMA. I am especially grateful to Philippe Veysseyre and Jean-Francois Escuret, who supported me to go to MIT and to Alain Madec, my internship tutor. The preparation I received during my internship at SNECMA has often been a key factor of progress for the research. The encouragement and the flexibility they granted me have always been very helpful.

I am also very much indebted with Dr Choon S. Tan of the Gas Turbine Laboratory, who has been a patient and supportive advisor during the 16 month of my research. I have always appreciated the freedom he gave me to conduct the research and his availability to answer my numerous questions.

I also would like to thank the faculty staff of the Gas Turbine Laboratory. In particular, I want to thank Paul Warren, Lori Martinez and Holly Anderson who are making our life easier day after day.

It is not possible to conduct a research without the help of co-researchers and I am especially grateful to Sanith Wijesinghe, who helped me a lot at the start of my research. He introduced me to Hoying's code. His patience has been a lesson to me. I want to thank Huu Duc Vo with whom I worked closely all along the research. His enthusiasm and imagination have always been very supportive.

Finally, I want to express my love and gratitude to my parents and I want to apologize for me being so far away for such a long time. This thesis is dedicated to them and I still think about the gardener hut.

Contents

List of Figures

List of Tables

NOMENCLATURE

Symbols

c	Blade chord
d	Spacing of counterrotating vortices
e	Energy
h	Blade spacing
	Height of counterrotating vortices above flat plate
i	$\sqrt{-1}$
k	Index of summation
l	Moment arm length
l_1	Upstream extent of flat plate pressure distribution
l_2	Downstream extent of flat plate pressure distribution
p	Static pressure
r	Distance from line vortex
s_1,s_2	Constants in expression for counterrotating vortex strengths
t	Time
u	Velocity in axial direction
v	Velocity in azimuthal direction
v_f	Fluid flux velocity in azimuthal direction
w	Wake width
	Induced velocity
x	Axial direction coordinate
y	Azimuthal direction coordinate

y^+	Boundary layer coordinate $(\sqrt{\tau_w/\rho y})/\nu$
A_{eff}	Effective area used in cascade model
C_μ	Turbulence model constant
C_1	Turbulence model constant
C_2	Turbulence model constant
Cf	Wall skin friction coefficient
Cm	Moment coefficient about mid chord (positive clockwise)
Cp	Pressure coefficient
ΔCp_s	Static pressure rise coefficient across the shock wave
Cx	Axial force coefficient
Cy	Azimuthal force coefficient
K	Constant of proportionality in cascade model
M	Mach number
N	Number of discrete vortex panels
R	Gas constant
Re	Reynolds number
St	Strouhal number
T	Flat plate cascade spacing
U	Total velocity
U_R	Rotor tip speed
U_{edge}	Boundary layer edge velocity at blade trailing edge
α	Angle between flow and flat plate
β_1	Flat plate stagger angle
δ^*	Boundary layer displacement thickness
η	Coordinate normal to flat plate
γ	Ratio of specific heats ($\gamma = 1.4$)
λ	Position of density discontinuity
μ	Reduced frequency (fc/U)
	Viscosity
ν	Kinematic viscosity
ω	Vorticity
ρ	Density

ρ^*	Density parameter $(\rho_2 - \rho_1)/(\rho_2 + \rho_1)$
Ψ_{s-s}	Static to static pressure rise coefficient
ξ	Coordinate along flat plate
σ	Flat plate cascade space–chord ratio (T/c)
σ_κ	Turbulence model constant
σ_ϵ	Turbulence model constant
θ	Boundary layer momentum thickness
τ	Non dimensional time
τ_w	Wall shear stress
ϑ	Blade trailing edge thickness
ζ	Location of any point in the complex plane $(\zeta = \xi + i\eta)$
Γ	Circulation strength
Γ_A	Circulation strength of counterrotating vortex A
Γ_B	Circulation strength of counterrotating vortex B
Γ_k	Circulation strength of vortex panel k
Γ_{max}	Maximum circulation strength of counterrotating vortices

Subscripts

1	Free stream or value outside density wake
2	Value inside density wake
	Behind density discontinuity for Marble's analysis
∞	Free stream value or total value

Operators and Modifiers

$\widetilde{()}$	Non–dimensionalized quantity
Δ	Difference operator
∇	Gradient operator

Acronyms

HCF	High Cycle Fatigue
CFD	Computational Fluid Dynamics
DFT	Discrete Fourier Transform

CHAPTER 1

INTRODUCTION

1.1 Background

Aircraft engine companies maintain their competitive edge by striving to design engines according to a certain number of criteria: reduced weight, reduced complexity, improved fuel consumption/thrust ratio, lower emissions among others. The effort to reduce weight in particular is impacting the number of stages of the compressor or the turbine of modern engines. The goal is to develop a higher-pressure ratio compressor with less blade rows. This also means lower manufacturing costs and fewer parts. A limiting factor in the design of such higher performance compressors is the onset of aerodynamic instabilities that limits the engine useful operating range. This is the reason why designers have to introduce a safety margin for the placement of the operating point on the compressor performance map. As we can see in Figure 1-1, inlet distortions can have an impact on the surge line. This effect requires a higher stall margin. In order to find the most adequate surge margin, it is essential to understand what are the parameters impacting the surge line and what are the mechanisms leading to instability. The scope of this thesis is to assess the feasibility of integrating the stability analysis into the compressor design loops. Creating a tool to assess the performance of a compressor stage or a group of stages in terms of stability even before it is made has the potential to reduce the development time by reducing the number of iterations during the design of high performance compressors.

In this chapter, we will undertake a review of the current status of compressor insta-

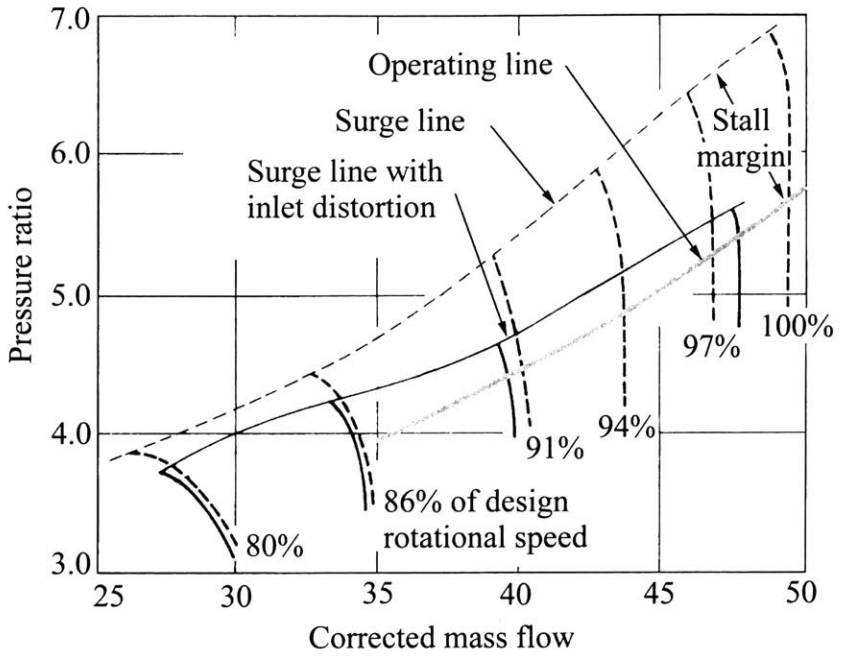

Figure 1-1: Compressor performance map and the effects of inlet distortions [21].

bilities and the models for stability assessment. This is then followed by a delineation of the contributions of this thesis.

1.2 A Review on Compressor Instabilities

1.2.1 Three Types of Compressor Instabilities

Based on observations, three types of instabilities can be defined when the operating point crosses the surge line: progressive stall, abrupt stall and surge (Figure 1-2). Progressive stall can happen when the compressor operates at a speed below the design speed. As the flow coefficient is reduced, the pressure rise decreases gradually. Figure 1-3(a) shows the patterns of the low flow rate regions that increases in size as the flow coefficient decreases. A sudden pressure drop at the peak of the pressure rise characteristic characterizes abrupt stall. The shape of the curve is due to a sudden stalling of an important portion of the row which instantly drops the pressure rise (Figure 1-3(b)). The stalling impacts every stage of the compressor. Unlike progressive stall, the non-linearity of this pattern prevents the operating point from going back and forth on the same line. To recover to a stable state, the flow rate has to be increased past the point of instability, hence the observed hysteresis.

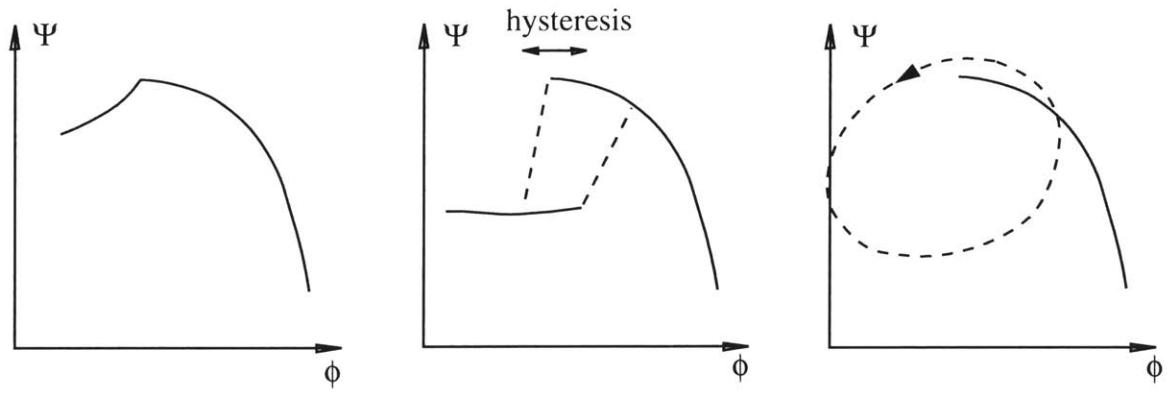

Figure 1-2: Three types of compressor instability characterized in terms of the respective pressure rise characteristics.

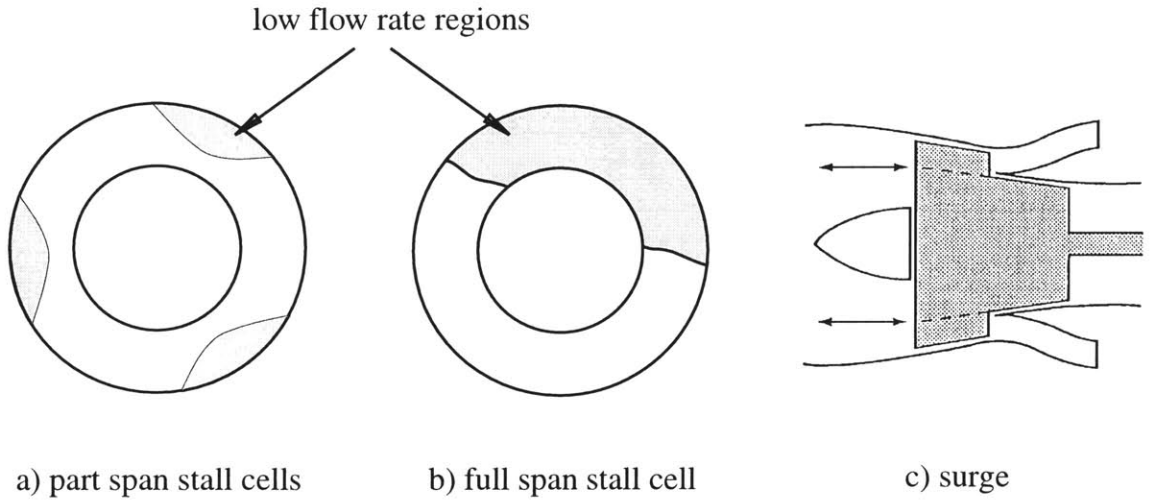

Figure 1-3: Three typical instability patterns in compression systems.

Surge appears when the conditions allow the compressor to be coupled with the combustor to become a resonator. The flow then oscillates axially, back and forth along the entire length of the engine. This can result in the propagation of the flame to engine intake and exhaust.

1.2.2 The Onset of Instability

The formation of compressor instabilities consists of three stages: (1) inception; (2)development; and (3) fully stalled flow pattern. If we want to have a good understanding of these instabilities, it is critical to focus on their onset. The point where the system no

longer damps the disturbances defines the last operating point. These disturbances could be associated with phenomena such as casing boundary layer, tip leakage flow, boundary layer separation or a combination of any of these. The final form of instability can be either rotating stall or surge. In some cases, rotating stall can lead to surge [9].

1.2.3 Rotating Stall propagation

Emmons [8] was the first to delineate the mechanism that underlies the propagation of rotating stall pattern around the annulus as shown in Fig 1-4 . The high blockage created inside one blade passage redistributes the flow upstream of the row. This creates a high incidence angle ahead of the stall propagation direction and a low incidence behind. The result is the stalling of the blades that are ahead of the disturbance and a reduced loading on those behind which recover from previous stall. The stalling pattern moves in the same direction as the rotor but at a lower speed . Therefore, in the absolute frame the arrow for the propagation of stall would be in the direction opposite to that of the rotor. Cumpsty and Greitzer [5] have modeled the rotating stall propagation as a result of the balance between the unsteady inertial effects in rotors and those in stationary components. They could correctly predict the measured speed of rotating cells showing that inertial effects have a major impact on the propagation mechanism. Longley [15] demonstrated that flow redistribution upstream of the row also contributes to the rotating speed of the stall cells in addition to the inertial effects.

1.2.4 Stall inception types

Experiments have distinguished two types of stall inception: modal waves and spikes. Modal waves is a linear phenomenon which is characterized by exponentially growing disturbance waves whose length scale is in the order of the annulus of the rotor. Its rotating speed ranges between 20% and 50% of the rotor speed. It is possible to record velocity traces by probes placed around the annulus during the development of the instability (Figure 1-5). These waves span the axial extent of the compressor and they have little variation from hub to tip. They can be detected by sensors at any location within the compressor. The Moore-Greitzer model [19] can predict the pre-stall modal waves observed in experiments. Spikes

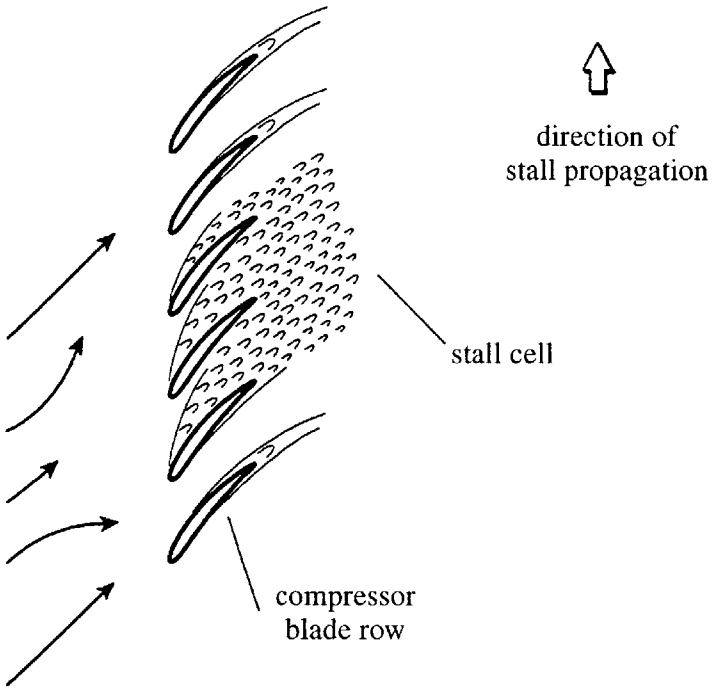

Figure 1-4: Emmons's rotating stall cell propagation mechanism.

are defined as localized short wavelength non-linear disturbances. They are associated with "short wavelength stall inception". As for modal waves, Figure 1-6 shows the velocity traces during a compressor stalling through spikes. The formation of one or several spike-shaped finite amplitude disturbances in the tip region of a particular stage starts the process. After three or five rotor revolutions, the disturbance develops into a full span stall cell. The initial rotating speed of this type of disturbances is around 70% of the rotor speed and as it evolves into a fully developed stall cell, the speed decreases to the final value of 0.2-0.4 rotor speed.

1.3 Review on short wavelength stall inception experiments

1.3.1 Effect of Inlet Distortion

Longley et al [16] have studied the impact of rotating inlet distortions on compressor stability and found that there are two types of compressor responses. Either there is one resonance peak corresponding to a minimum of stall margin when inlet distortion is rotating at 0.4 rotor speed (Fig 1-7(a)) or there are two resonance peaks at 0.3 times the rotor speed and

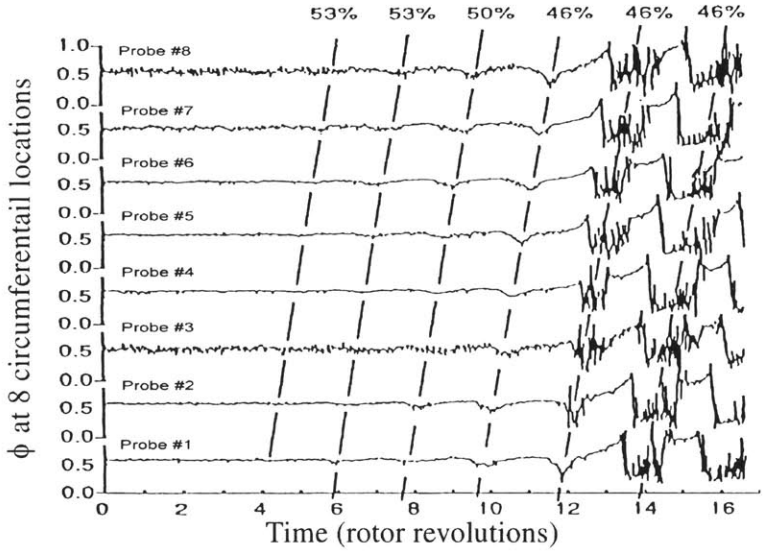

Figure 1-5: Velocity traces of eight sensors on the annulus show a typical stall inception through modal waves [17].

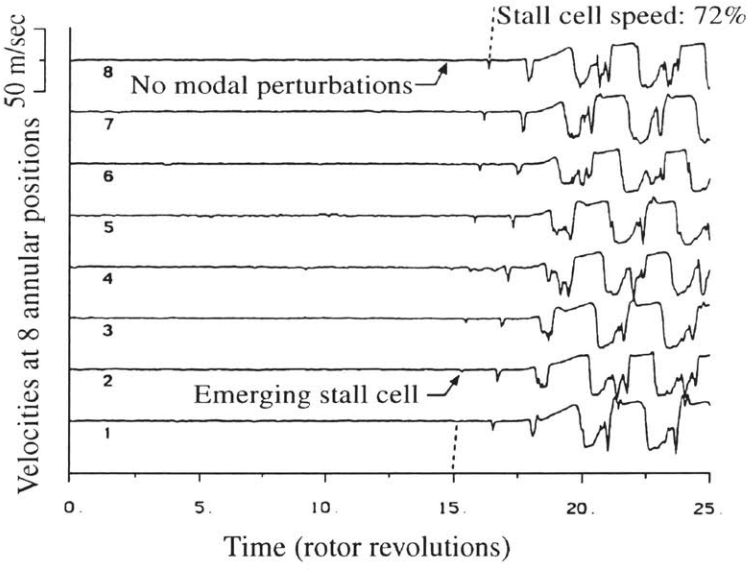

Figure 1-6: Velocity traces of eight sensors on the annulus show the compressor stall inception through short wavelength disturbances (spikes) [6].

0.75 times the rotor speed (Fig 1-7(b)). In the first case, the compressor stalls through modal waves while in the second it stalls through spikes. Therefore each compressor has a characteristic stall pattern which corresponds to two stall inception mechanisms. The rotating stall disturbances can have a different impact on the stall margin depending on the compressor.

1.3.2 Conditions for short wavelength stall inception

Camp and Day [1, 2] have experimented one compressor with different IGV stagger angles. They observed that the stall points line up at a constant rotor tip incidence whenever the compressor stalls by spike inception(Fig 1-8). It is therefore possible for one stage to stall either by modes or by spikes depending on the IGV stagger angle. They noticed that as the compressor was more loaded, it had the trend to stall by spikes rather than by modes and the first stage played a key role in the inception pattern.

Their conclusion was the existence of a unique rotor tip incidence as a short wavelength stall criterion (Fig 1-9). If this incidence is reached on the negative slope portion of the pressure rise characteristic, the compressor will stall by spikes, if not it will stall by modes at the peak of the pressure rise characteristic.

1.4 Review of compressor stability models

From the point of view of the designer, it is crucial to adequately describe the stability of the compressor so as to be able to predict the stability margin. A concise review of the state of compressors stability models is given in the following.

1.4.1 Maximum of the characteristic as an instability criterion

This criterion proposed by Dunham [7] was that compressor instability occur at the peak of the total-to-static pressure rise characteristic corresponding to the zero slope. Figure 1-10 shows the effect of the compression system on a small perturbation of the axisymetric flow field. If the operating point is on the negative slope portion of the pressure rise

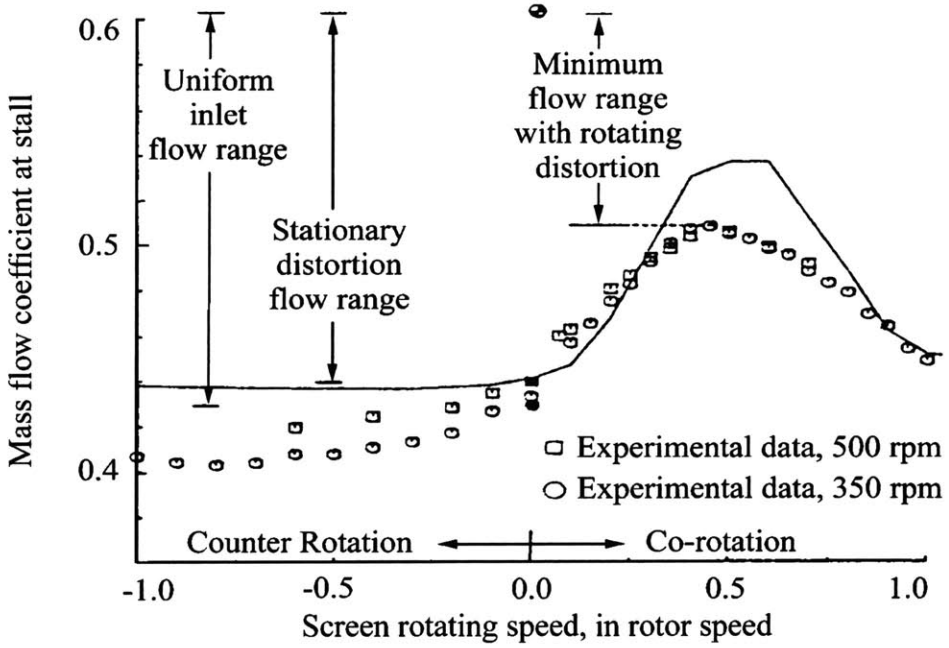

(a) Single resonance peak

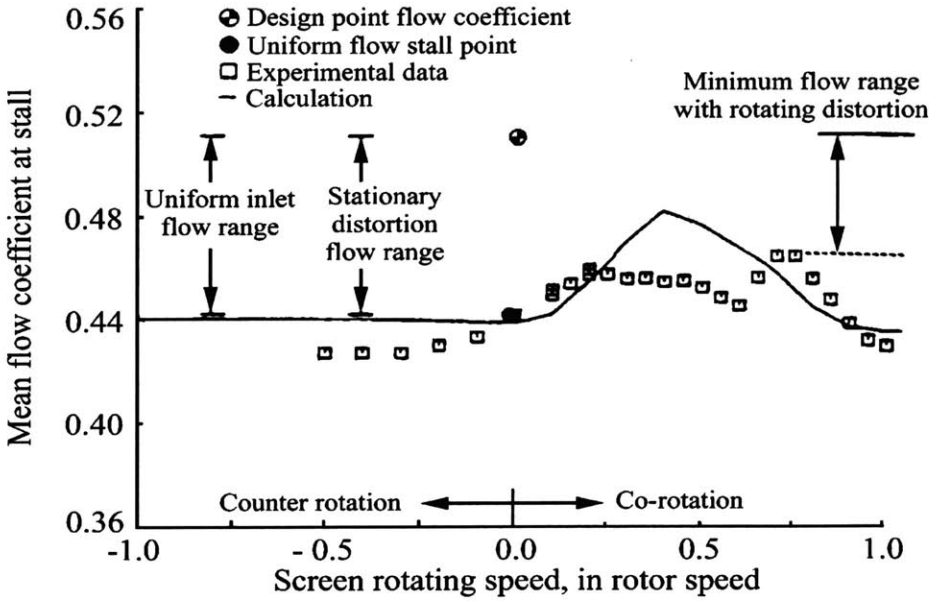

(b) Two resonance peaks

Figure 1-7: Two types of compressor resonance response to rotating inlet distortions.

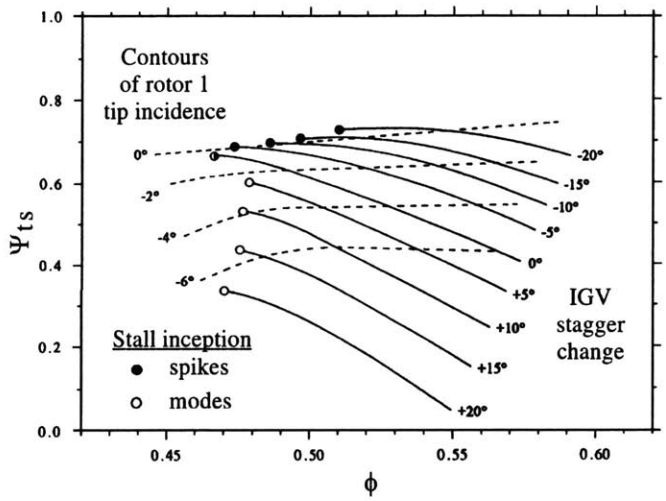

Figure 1-8: Unique rotor tip incidence for spike stall inception.

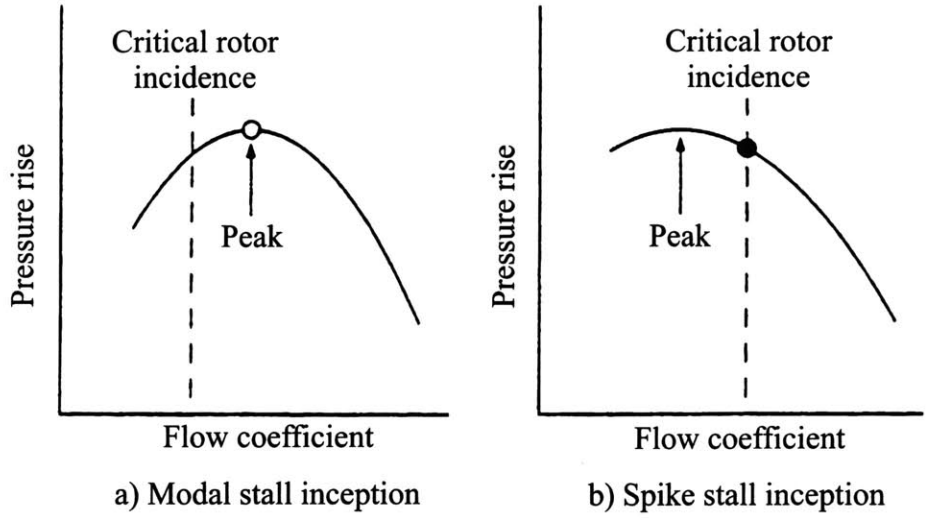

Figure 1-9: A model for determining the stall inception type of a compressor [2].

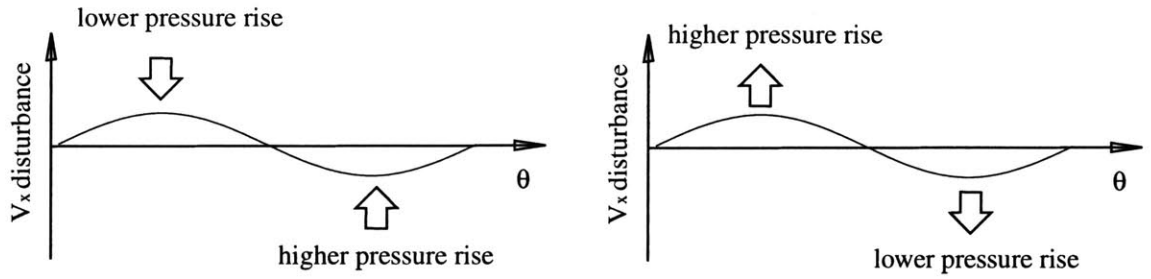

a) A disturbance is suppressed by the compressor in negatively sloped characteristic region

b) A disturbance is amplified by the compressor in positively sloped characteristic region

Figure 1-10: Influence of slope of compressor pressure rise characteristic on stability of disturbances.

characteristic and the flow gets accelerated locally, it results in a bigger pressure rise and this slows the flow and vice versa. This portion of the characteristic is declared stable. On the positive slope portion of the characteristic, if the flow accelerates locally, the effect is now a decreased pressure rise, which accelerates the flow even further. This portion of the characteristic is unstable. Dunham's model doesn't take into account the rotational effects of these disturbances while it has been shown in later models [4, 20] that it can slightly impact the instability point.

1.4.2 The Moore-Greitzer model

Using a lumped compressor representation with an axisymetric pressure rise characteristic, Moore was able to accurately model the rotating speed of stall cells. He could also reproduce the zero-slope criterion of total-to-static pressure rise characteristic as the neutral stability point. Moore and Greitzer [19] have developed an approximate theory for general post-stall transients in axial compression systems. Their model was able to describe the strong coupling between surge-like and rotating-stall-like oscillations. They have carried out calculations for post-stall transients which involved the growth or decay of stall cells and they found that the instantaneous rotating stall-cell amplitude has a significant effect on the instantaneous compressor pumping characteristic and therefore on the overall system response.

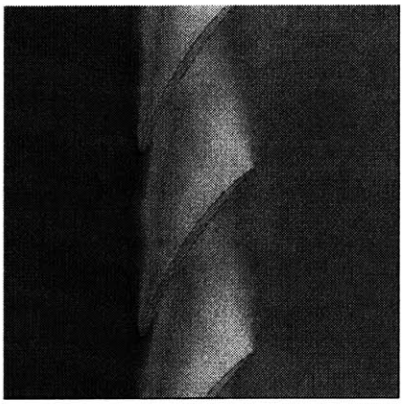

Figure 1-11: Vorticity contours in the blade passage flow.

1.4.3 CFD models

Since rotating stall phenomena like part-span stall and short-wavelength stall inception are three-dimensional and non-linear in nature, 2-D linear models are inadequate for delineating flow features associated with such instabilities. Current availability of computational resources now permits the solution of Navier-Stokes equations for potential resolution of technical issues connected with 3-D stalling behavior.

1.4.4 Donald Hoying's model

Hoying developed a code called RS3, which performs this kind of calculations. This is one of the codes that will be used to study the instability behavior of the compressor examined in this thesis. Using this code, Hoying et al [13], found that the tip leakage vortex position in the blade passage is critical for the development of stall cells in the tip region. Computing the flow field at the tip region for several settings of the throttle, it is possible to show the trajectories of the tip clearance vortices as the flow coefficient reduces (Fig 1-11) . The rotor blade geometry used for this calculation was the one of the E^3 rotor with 3.0% tip clearance. Figure 1-12 shows how the clearance vortex trajectory becomes perpendicular to the axial direction.

The presence of a solid boundary induces an upstream self-induced velocity associated

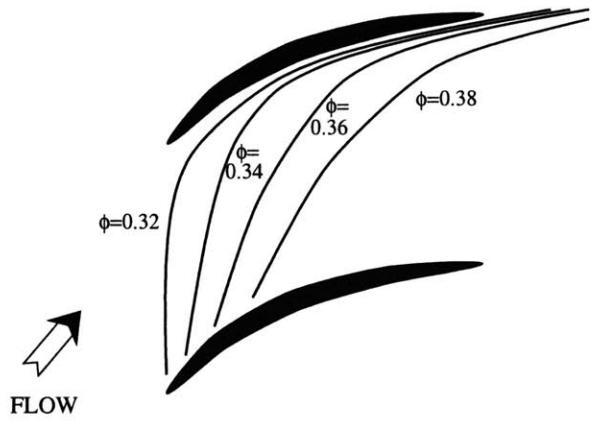

Figure 1-12: Trajectories of the tip clearance vortex for the E^3 rotor with 3.0% tip clearance for different flow coefficients.

with the vortex that can be explained by the idea of an image vortex as shown in Figure 1-13. There is a balance between the mean flow velocity and the velocity associated with the vortex that determines their trajectory. If the vortices impact the adjacent blade behind the leading edge, a local perturbation of the mean flow will not affect this equilibrium in the long term. But if the trajectory of the vortices is perpendicular to the mean flow, the system stands on a bifurcation point. If there is a small perturbation in the upstream flow, the tip leakage vortices will move forward in the blade passage leading to an unstable flow situation. The criterion based on the results of Hoying's computational experiments has been inferred under the assumptions and approximations for which his computations have been implemented. This criterion has been under contention recently. The weakness in Hoying's calculations was the assumption of inviscid casing walls. Recent experiments and calculations by Seitz [22], Van Zante [26] and Vo [27] appear to indicate the impact of casing boundary layer on the behavior of tip vortex and stall inception. More recently Vo has called into questions the manner in which the computed solutions in [11] and [12] have been interpreted.

1.5 Technical objectives

Nowadays, engine companies cannot afford as many iterations in the design of their compressors as they did 10 years ago. Their goal is to have a successful design in one design iteration. A primary objective of this study is to suggest and explore a framework for im-

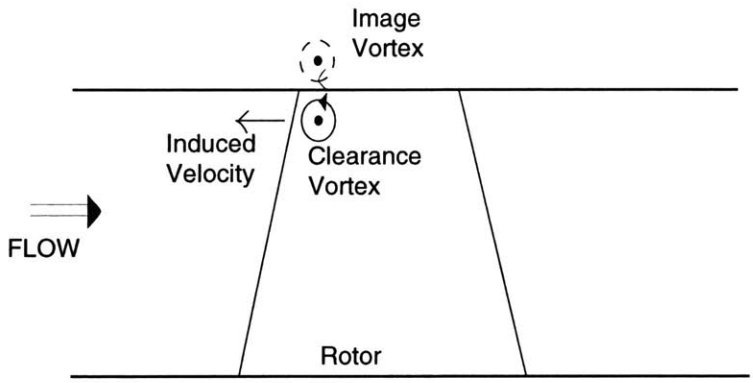

Figure 1-13: Velocity induced by image vortex.

plementing a compressor stability analysis during the design process of a new compressor. The geometry used for the study is a research compressor from an engine manufacturer. At the time of this study, the compressor has not been built and the only data available were taken from axisymetric calculations. The analysis of the key design characteristics that affect the instability point and its inception type will yield a set of recommendations for future modifications in the design of a more stable compressor. In addition, we would like to determine if this compressor would experience spike-inception rotating stall and if the trajectory of tip leakage vortices is a key feature that triggers the inception of stall or if it is only a result of the instability.

1.6 Overall approach

The first step of the process is to modify Hoying's code so it can be used to calculate flow in compressor flow path with varying hub. The modified code will be used to generate the pressure rise characteristics of each of the four blade rows. These computed results will then be used to develop the row-by-row body force representation of the compressor so as to enable the implementation of Gong's type of stability calculations [11].

With the body force representation, the stability behavior can be assessed for changes in operating conditions as well as design parameters.

In parallel with the stability assessments based on body force representation of compressor, 2-D calculations are implemented to provide conditions for the implementations of

3-D calculations based on Hoying's rs3 code for establishing the peak of the pressure rise characteristic and the corresponding throttle position. This is then followed by the implementation of an 11-blade-passage unsteady 3-D flow simulation to determine the detailed flow features responsible for initiating the stalling of the compressor

CHAPTER 2

PRELIMINARY 2D CALCULATIONS

2.1 Introduction

As the 2 stage High Pressure ratio compressor constitutes an experimental compressor that has not been built, we have no experimental data. Axisymmetric calculations have been carried out to generate the speed line. Midspan 2D calculations have been implemented to generate the pressure rise characteristic for each blade row. As it is a high-speed compressor, there is a possibility to have flow choking in the blade passage. The tool used for this set of calculations is the two-dimensional, time accurate, explicit Navier-Stokes flow solver developed by Donald Hoying called RS2. We will first give a concise description of this CFD code and the input data needed for implementing the calculations (computational grid, boundary conditions and the variables used to non dimensionalize the results). Computed results are then described and their implications discussed.

2.2 Characteristics of RS2

The RS2 code is based on the use of:

1. Finite difference discretization.
2. Fourth–order spatial accuracy and third–order temporal accuracy.
3. Dispersion Relation Preserving (DRP) scheme (Tam and Web [25]).

4. κ–ϵ turbulence model.

5. Wall functions (Chieng and Launder [3]).

6. Non–reflecting inlet and exit boundary conditions (Giles [10]).

The phenomena appearing during the rotating stall involve a large range of length scales. As the flow under investigation is unsteady, the code has to deal also with a large range of time scales. The study of rotating stall requires codes that can preserve the dispersive characteristics of wave-like phenomena. Such codes will accurately simulate the propagating speed of any frequency detected in experiments. These frequencies can be high for events associated with short wavelength stall inception and low in the case of modal wave stall inception. In order to reduce dissipative and dispersive errors of his model, Hoying implemented a Dispersion Relation Preserving scheme. The details of the implementation can be found in Hoying [12].

Assuming that the viscous effects of the flow are confined in the region close to the blade, Hoying decided for computational cost reasons to use two superimposed grids: an underlying H-grid where the Euler equations are solved and a O-grid around each blade where the Reynolds-Average Navier-Stokes equations are solved. An example of the computational domain used is shown in the Figure 2-1. A standard two equation κ–ϵ turbulence model is implemented using the following constants:

$$C_\mu = 0.09,\ C_1 = 1.44,\ C_2 = 1.92,\ \sigma_\kappa = 1.0,\ \sigma_\epsilon = 1.3 \tag{2.1}$$

Launder and Spalding [14] have found those coefficients to be appropriate for free shear flows and flows near solid boundaries.

In order to further reduce the computational grid needed and therefore the time of calculations the model uses wall functions to model the inner portion of the blade boundary layers where the shear stress is constant. The first near wall grid point can be located at $y^+ \approx$ 30–150. The solid wall boundary conditions are modified by the wall functions such that the correct viscous stress is calculated without the necessity of computing the

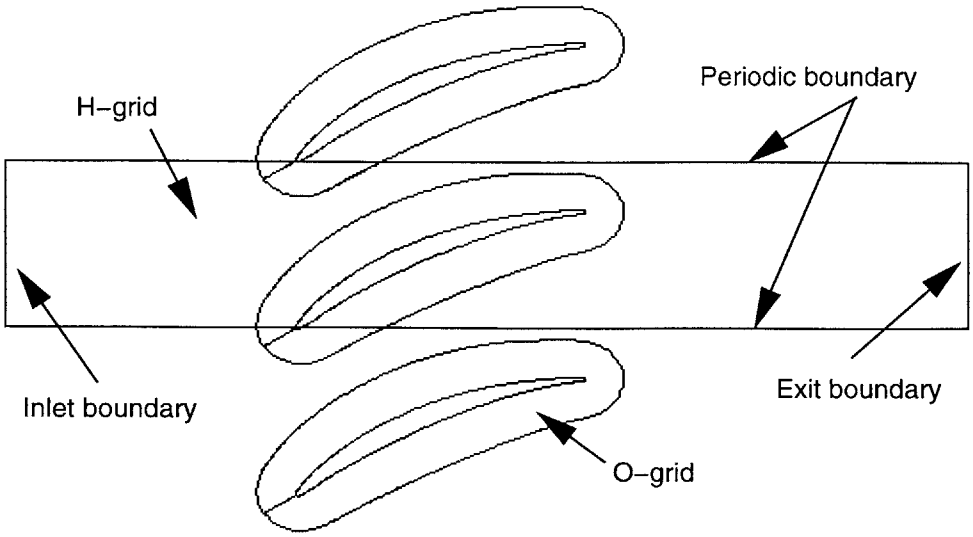

Figure 2-1: Schematic of the computational domain and boundary conditions.

boundary layer flow details at the wall.

At the exit and the inlet of the computational domain, non-reflective boundary conditions developed by Giles [10] are used.

2.3 Non-Dimensionalization

The reference variables used in the non-dimensionalization of the problem are:

- Length : blade spacing (s)
- Velocity : rotor tip speed (U_R)
- Density : free stream density (ρ_∞)
- Temperature : free stream temperature (T_∞)
- Viscosity : free stream viscosity (μ_∞)
- Pressure : $\rho_\infty U_R^2$
- Energy : U_R^2

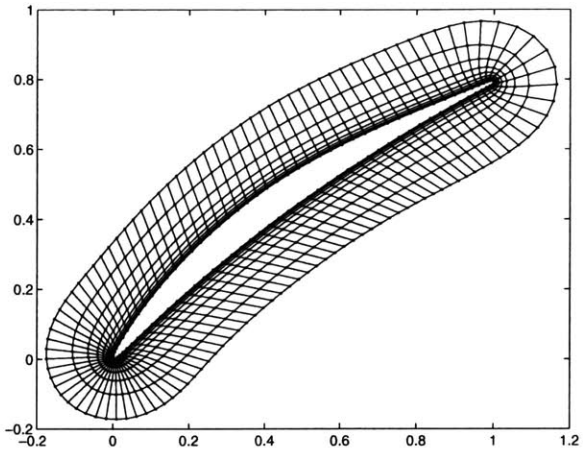

Figure 2-2: Example of the O-grid used.

2.4 Computational Grid

As alluded to in the above there are two overlapping H and O grids. The H-grid has uniform spacing in the two directions in order to simplify the calculation of numerical derivatives. The H-grid characteristics are chosen in order to simulate an inlet and an outlet duct. The O-grid is generated by an elliptic partial differential equation method developed by Steger and Sorenson [24]. This method allows for high-density grid around the leading and the trailing edge of the blade for resolving high gradients in those regions. The lines of the O-grid are perpendicular to the surface of the blade, which helps to simplify the numerical evaluation of normal derivatives. The factor that limits the number of points for the O-grid was the CFL number for which the code would diverge. The trade-off between computer time and convergence for the first rotor of the geometry led us to choose a grid of 157 points around the blade surface and 13 nodes radially. The H-grid has 81 points in the azimuthal direction and 449 points in the axial direction. Figure 2-2 shows the O-grid for the first rotor.

2.5 Variable hub radius

The original version of RS2 has been written for low speed compressors where the hub geometry had a constant radius. The present compressor's geometry has a varying hub radius. Thus the code has to be modified accordingly as described in the next sections.

2.5.1 Quasi-Three-Dimensional Navier-Stokes Equations

In order to express the quasi-three dimensional viscous compressible flow along the axisymetric surfaces defined by the streamlines, we need to use an axisymmetric coordinate system (m,θ) which rotates with the blade row; m is given as:

$$dm^2 = dz^2 + dr^2 \tag{2.2}$$

If we denote r the radius and h the streamline thickness which are known functions of m, the Navier-Stokes equations may be expressed in the following form:

$$\frac{\partial(rh\vec{U})}{\partial t} + \frac{\partial(rh\vec{F})}{\partial m} + \frac{\partial(h\vec{G})}{\partial \theta} = \frac{\partial(rh\vec{R})}{\partial m} + \frac{\partial(h\vec{S})}{\partial \theta} + rh\vec{K} \tag{2.3}$$

where

$$\vec{U} = \begin{pmatrix} \rho \\ \rho V_m \\ \rho V_\theta r \\ \rho E \end{pmatrix}, \vec{F} = \begin{pmatrix} \rho V_m \\ \rho {V_m}^2 + p \\ \rho V_m V_\theta r \\ V_m(\rho E + p) \end{pmatrix}, \vec{G} = \begin{pmatrix} \rho W_\theta \\ \rho V_m W_\theta \\ (\rho V_\theta W_\theta + p)r \\ W_\theta(\rho E + p) + r\Omega p \end{pmatrix}, \tag{2.4}$$

$$\vec{R} = \begin{pmatrix} 0 \\ \sigma_{11} \\ \sigma_{12} r \\ R_4 \end{pmatrix}, \vec{S} = \begin{pmatrix} 0 \\ \sigma_{12} \\ \sigma_{22} r \\ S_4 \end{pmatrix}, \vec{K} = \begin{pmatrix} 0 \\ K_2 \\ 0 \\ 0 \end{pmatrix} \tag{2.5}$$

These equations have been reimplemented in the code. Since the preliminary axisymetric calculations could show the streamlines of the flow, one could implement in the code a function giving the local radii and streamline thickness to be used in the preceding equations. Figure 2-3 shows a θ constant cut of the calculation domain and two of the

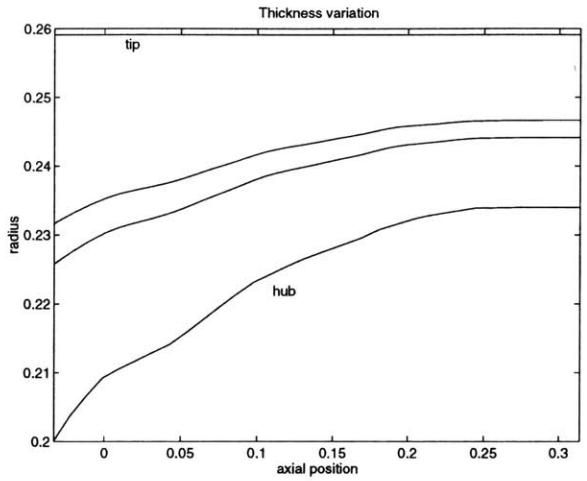

Figure 2-3: Streamline thickness.

streamlines. These streamlines are calculated as interpolations of the hub and tip lines. The hub line is given by the industrial design and contains changes of slopes for industrial reasons therefore the interpolated lines used to calculate the streamline thickness also contain these changes of slope even if they are not physical.

2.6 Comments on implementation

2.6.1 Method used

This first set of calculations was designed to give us an idea of the flow behavior in each of the blade rows of this research compressor and in particular their pressure-rise characteristic. First we have to get the steady-state flow. The rotating speed is set to the design value of: 1208.8 rad/sec. The backpressure is set by the throttle. As the throttle is reduced the backpressure rises and the mass flow reduces. We can then obtain operating points that will give us the operating pressure rise characteristic. It is important to stress that the change of throttle was continuous during the calculation since we have first reached a steady state. It is not possible to determine if the flow fields obtained are steady states but are affected by transient effects. However by stopping the change of back-throttle during the calculation one can show the difference between the transient point and the steady-point is less than 1% of the pressure ratio.

2.6.2 Boundary Conditions at Inlet of Computational Domain

The code implements inlet and outlet boundary conditions that prevent waves to be non-physically reflected on the boundaries of the domain. Donald Hoying validated his code for low-speed subsonic rotors but the situation being examined here is for a transonic compressor. As such the inlet boundary conditions was modified to account for the consistent propagation of flow information in the transonic flow situation.

2.7 Results

Figure 2-4 shows the static pressure ratio vs. the inlet mass flow. The first steady state point corresponding to a fully opened throttle gives a pressure ratio of 1.2 at a mass flow of 0.65. As the throttle is reduced, points are lining up almost vertically. If we look at Figure 2-5, we notice a normal shock in the blade passage and therefore the inlet conditions are not dependent on the throttle position. When the throttle is further reduced, the shock moves upstream and then vanishes. We can plot the Mach number field at the peak of the pressure rise characteristic in Figure 2-6 and we notice that the back 20% of the suction side are stalled. If we zoom in on that region and plot the velocity vectors in Figure 2-7 we see a recirculation region.

Figure 2-8 shows the Mach number during the transient to stall. We notice the separation region on the suction side of the blade and the recirculation region behind the trailing edge of the blade. There is an increase in the blockage of the flow in the blade passage.

Calculations have been carried out for each row of the compressor geometry and their computed characteristics are plotted in Figures 2-9, 2-10, 2-11, 2-12. The bottom line shown in the figures represents a computational transient before the calculation actually converges to the first steady state solution. Upon reducing the throttle, the pressure ratio increases to a value corresponding to the peak of the pressure rise characteristic, and then drops until a critical mass flow has been reached when the calculation becomes unstable.

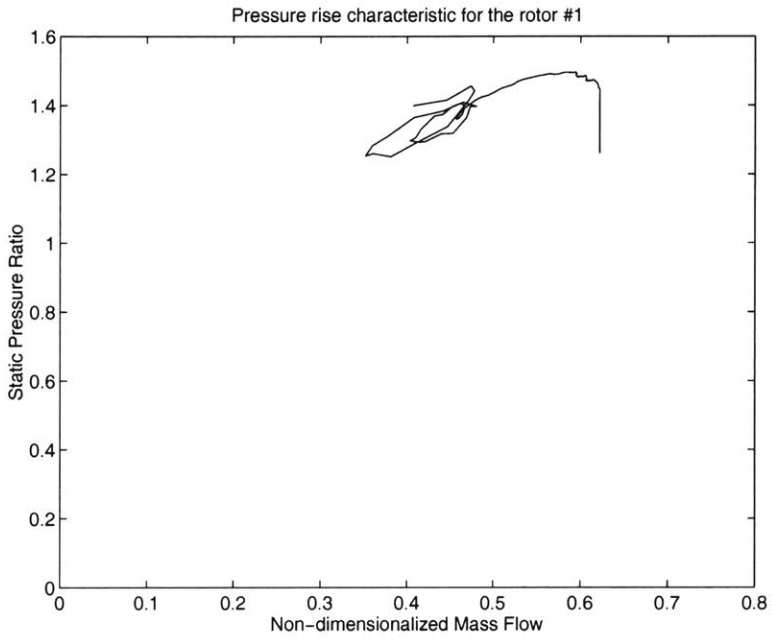

Figure 2-4: Static Pressure Ratio for rotor 1.

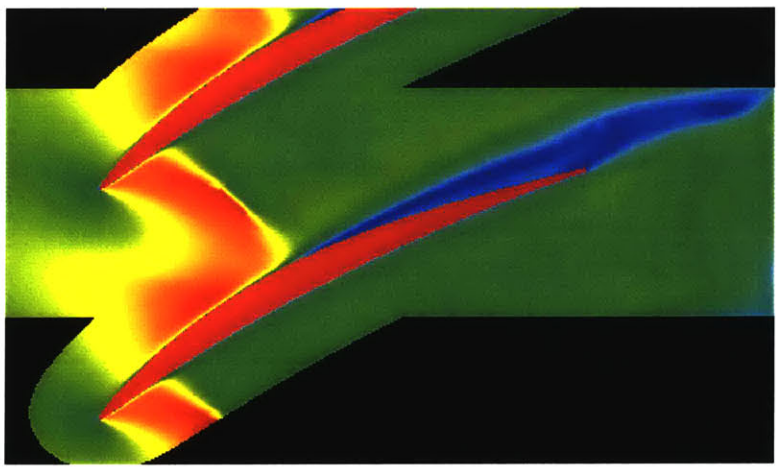

Figure 2-5: Mach number field for rotor 1.

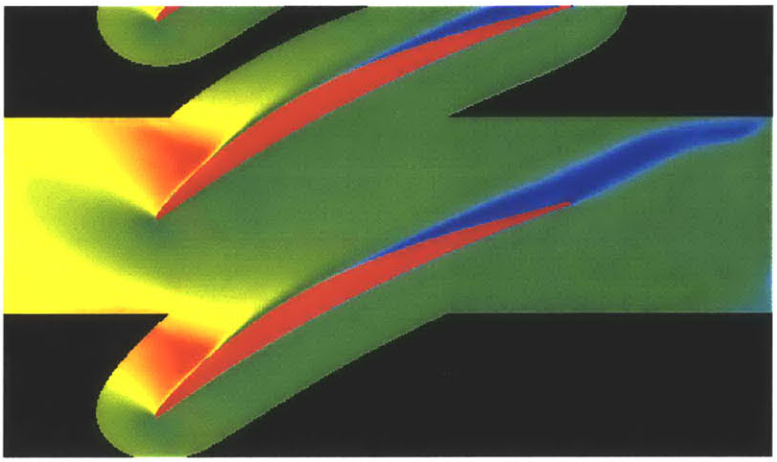

Figure 2-6: Mach number field for rotor 1 at the Peak of the Pressure Rise Characteristic..

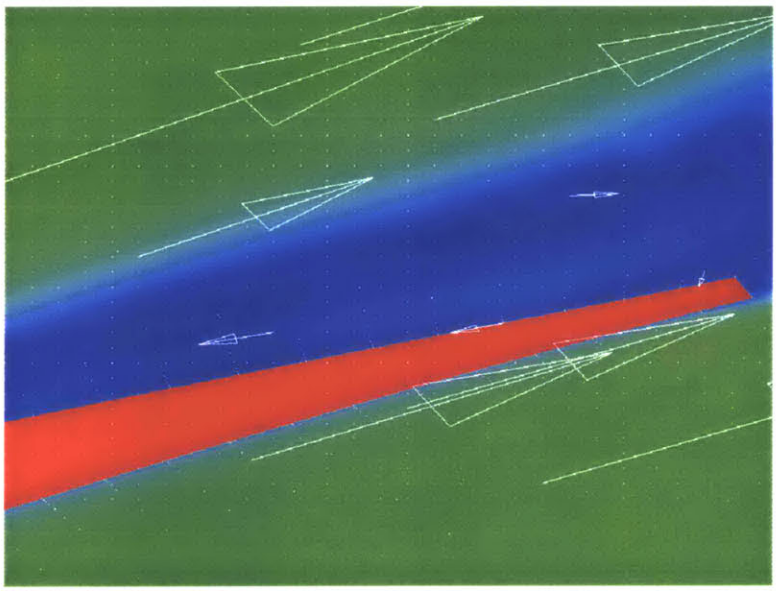

Figure 2-7: Recirculation region on the suction side of the Trailing Edge.

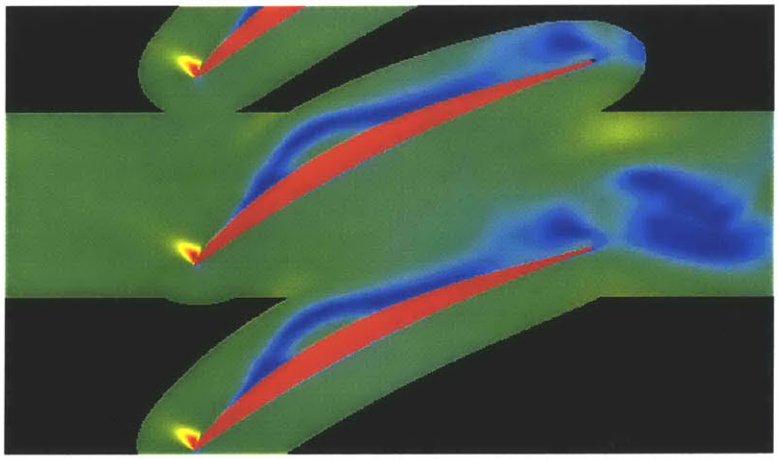

Figure 2-8: Mach number field for rotor 1 at stall.

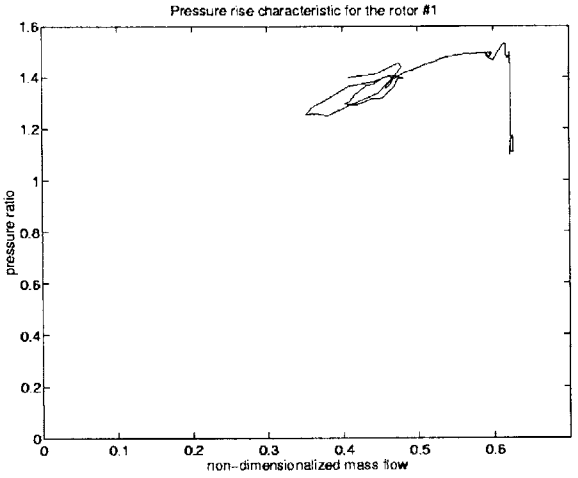

Figure 2-9: Pressure Rise Characteristic for Rotor1

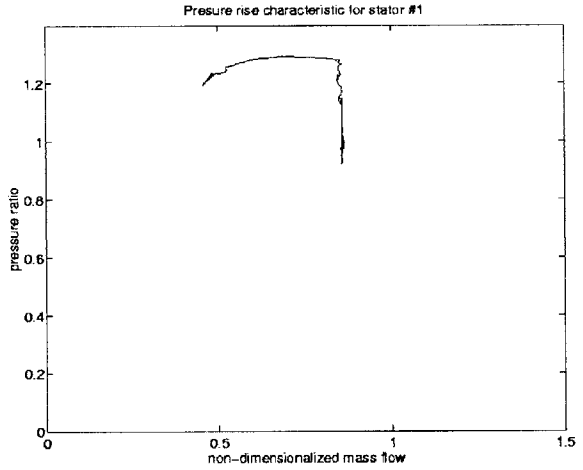

Figure 2-10: Pressure Rise Characteristic for Stator1

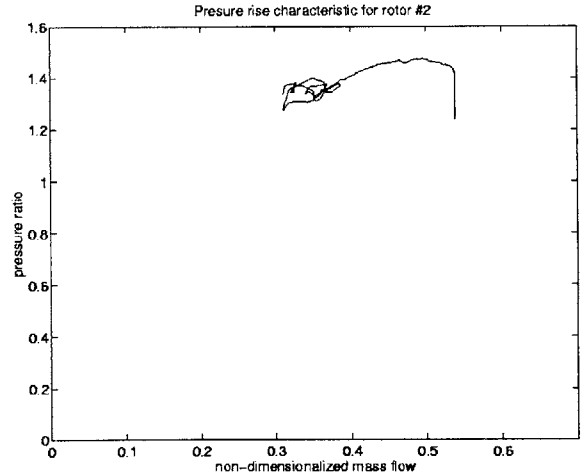

Figure 2-11: Pressure Rise Characteristic for Rotor2

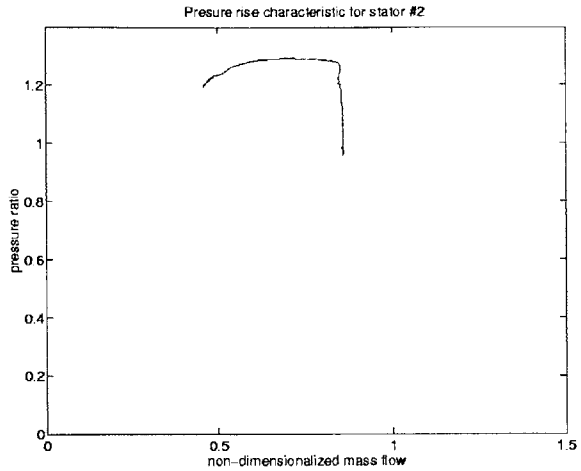

Figure 2-12: Pressure Rise Characteristic for Stator2

2.8 Summary

In this chapter, we presented computed results from the use of the 2-D version of Hoying's code: RS2. We have added a new feature to the code allowing it to compute flow in flow path with varying hub radius. The 2-D equations implemented had to be adapted to take into account the variation of the streamline thickness.

The implementation of inflow boundary conditions was modified for transonnic flow situations. The results showed the presence of a shock wave in front of the blade row and a recirculation region on the back of the suction side of blades.

CHAPTER 3

3D BODY FORCE REPRESENTATION OF BLADE ROW FOR STABILITY CALCULATION

3.1 Introduction

The 3D Navier-Stokes viscous solver allow us to simulate a wide range of length scales and the details of stall inception. The downside of such a solver is that the computation time required prohibits any parametric study on a practical basis. Thus a low order computational model that could reproduce the overall stability behavior of a compressor is needed. In this the method developed by Yfang Gong [11] is adopted. We will explain the key features of this method and demonstrate how it can potentially be used to implement a parametric analysis of the stability of our geometry.

3.2 The Blade Force Model

The compression system consists of an inlet and an outlet ducts, blade rows, a plenum and a throttle. Figure 3-1 shows the key elements in a compression system model.

The flow in the ducts and gaps is described by the unsteady three-dimensional inviscid Euler equations as:

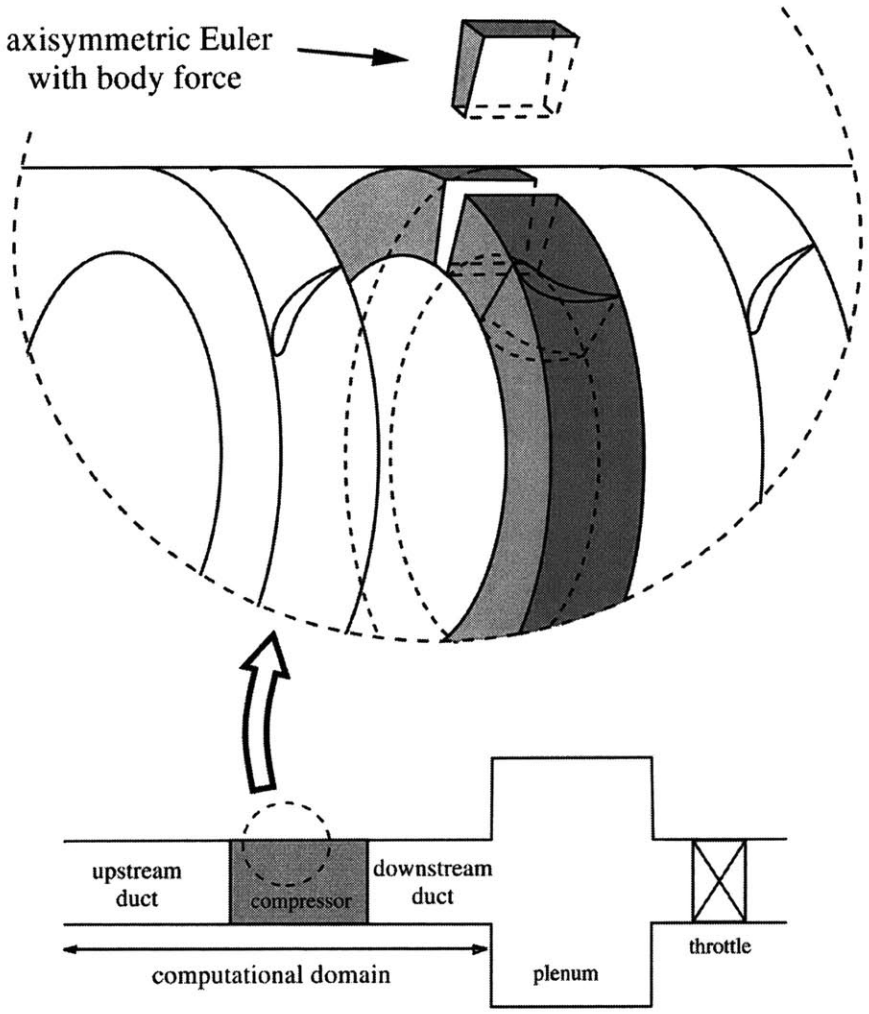

Figure 3-1: Compression system model and the blade row modeling

$$\frac{\partial}{\partial t}\begin{bmatrix} 0 \\ rV_x \\ rV_\theta \\ rV_r \end{bmatrix} + \frac{\partial}{\partial x}\begin{bmatrix} rV_x \\ rV_x^2 + rP/\rho \\ rV_xV_\theta \\ rV_xV_r \end{bmatrix} + \frac{\partial}{\partial \theta}\begin{bmatrix} V_\theta \\ V_xV_\theta \\ V_\theta^2 + P/\rho \\ V_\theta V_r \end{bmatrix}$$

$$+\frac{\partial}{\partial r}\begin{bmatrix} rV_r \\ rV_xV_r \\ rV_\theta V_r \\ rV_r^2 + rP/\rho \end{bmatrix} = \begin{bmatrix} 0 \\ 0 \\ V_\theta V_r \\ V_\theta^2 + P/\rho \end{bmatrix} \tag{3.1}$$

Each of the rows is represented by an appropriate body force representation (ie. infinite number of blade assumption). Thus the effects of the flow events within the blade passage can only be reflected in the body force representation. Flow events with length scale larger than a blade pitch can be described by such a model. Therefore, at each circumferential position, the flow is considered as axisymmetric and the pressure rise and turning due to the blade is reproduced by a body force field. Since we have an infinite number of blades, each circumferential position is independent from its neighbor and the three dimensional flow field is composed of an infinite number of axisymmetric flow fields as show in figure 3-1. The governing equations for the blade region are:

$$(\frac{\partial}{\partial t}+\Omega\frac{\partial}{\partial \theta})\begin{bmatrix} 0 \\ rV_x \\ rV_\theta \\ rV_r \end{bmatrix}+\frac{\partial}{\partial x}\begin{bmatrix} rV_r \\ rV_x^2+rP/\rho \\ rV_xV_\theta \\ rV_xV_r \end{bmatrix}+\frac{\partial}{\partial r}\begin{bmatrix} rV_x \\ rV_xV_r \\ rV_\theta V_r \\ rV_r^2+rP/\rho \end{bmatrix}$$

$$=\begin{bmatrix} 0 \\ F_x \\ V_\theta V_r+F_\theta \\ V_\theta^2+P/\rho+F_r \end{bmatrix} \tag{3.2}$$

where

$$(F_x, F_\theta, F_r)=\mathbf{F}(\mathbf{V}(x,\theta,r),x,r) \tag{3.3}$$

It is important to stress that this body force representation is dependent on local flow conditions in order to simulate flow redistribution within a blade row that happen during short wavelength disturbances. The flow properties which impact the body force distribution are the local Mach number M, deviation angle $\Delta\beta$ and Reynolds number Re. Therefore the force can be expressed as

$$\frac{h\mathbf{F}}{\rho V^2}=\mathbf{f}(M,\Delta\beta,Re)$$

with h is the local spacing of the blade passage as shown in Figure 3-2

For high Reynolds number flow, the body force can be expressed as:

$$\frac{h\mathbf{F}}{\rho V^2}=\mathbf{f}(M,\Delta\beta) \tag{3.4}$$

The model splits the body force into two parts (Marble [18]): $\mathbf{F}_n$ is the normal pro-

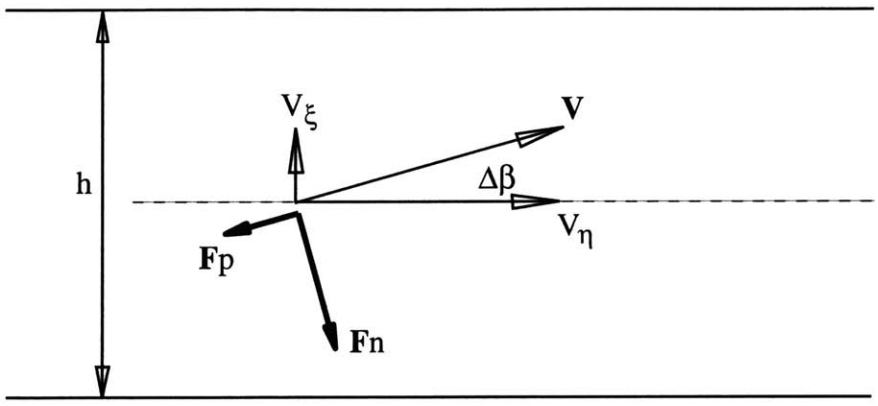

Figure 3-2: The flow in a blade passage is modeled as a flow in a straight channel locally.

jection of the force relative to the flow direction and $\mathbf{F}_p$ is the projection parallel to the flow direction in the relative frame. Therefore it is possible to formulate each component according to its physical basis. While $\mathbf{F}_n$ accounts for the work done by the blade row to the fluid through the pressure difference between the pressure and suction sides, $\mathbf{F}_p$ reflects the effects of the viscous force. The body force can therefore be expressed as:

$$\begin{aligned} \frac{h\mathbf{F}_n}{\rho V^2} &= f_n(M, \Delta\beta) \\ \frac{h\mathbf{F}_p}{\rho V^2} &= f_p(M, \Delta\beta) \end{aligned} \tag{3.5}$$

Eventually, the body force model relies on two coefficients $K_n(\Delta\beta, M)$ and $K_p(\Delta\beta, M)$ through

$$\begin{aligned} F_{n,x} &= \frac{K_n(\Delta\beta, M)}{h}\frac{V_\theta}{V}(V_x\cos\alpha + V_\theta\sin\alpha)(V_\theta\cos\alpha - V_x\sin\alpha) \\ F_{n,\theta} &= -\frac{K_n(\Delta\beta, M)}{h}\frac{V_x}{V}(V_x\cos\alpha + V_\theta\sin\alpha)(V_\theta\cos\alpha - V_x\sin\alpha) \end{aligned} \tag{3.6}$$

and

$$
\begin{aligned}
F_{p,x} &= -\frac{K_p(\Delta\beta, M)}{h} V V_x \\
F_{p,\theta} &= -\frac{K_p(\Delta\beta, M)}{h} V V_\theta \\
F_{p,r} &= -\frac{K_p(\Delta\beta, M)}{h} V V_r
\end{aligned}
\tag{3.7}
$$

Gong used coefficients that were based on data from measurements on NASA Rotor 35

$$K_n = 4.2 - 3.3 * \alpha$$

$$K_p = 0.04$$

but it has been necessary to conduct a parametric analysis to adapt these parameters to the present high-speed geometry. The criteria used is to choose the coefficients so as to match the maximum pressure ratio obtained from the axisymetric calculations. The details of such a procedure are presented in appendix A.

The fluid in the plenum is considered as uniform and isentropic and its dynamic are governed by the following equation:

$$\frac{dP}{dt} = \frac{\gamma\, P}{\rho\, V_{plenum}} (m_c - m_t) \tag{3.8}$$

with m_c denoting the flow rate from the compressor and m_t the mass flow rate through the throttle and V_{plenum} the volume of the plenum. The throttle pressure drop is given as :

$$\frac{P - P_{ambient}}{\rho U^2} = K_t \phi^2 \tag{3.9}$$

Since the situation examined here is unrelated to compressor surge, the plenum volume has been set to zero. The equations become:

$$\frac{P_{exit} - P_{ambient}}{\rho U^2} = K_t \phi^2 \tag{3.10}$$

where P_{exit} is the static pressure at the exit of the computational domain.

3.3 Stage pressure characteristics

3.3.1 Introduction

It is important to stress that we have only carried out axisymmetric calculations for use in determining the operating point at which the compressor would become unstable. Therefore, non-linear phenomena like 'spikes' have not been simulated as was done in Gong's thesis. For this study, we define our stability limit to be the peak of the pressure rise characteristic.

3.3.2 Evaluation of coefficients Kn and Kp

From Appendix A, the new set of coefficients for correlating the body force terms of the local flow conditions is:

$$K_n = 0.8 * (4.2 - 3.3 * \alpha)$$

$$K_p = 0.005$$

3.3.3 Most unstable row

In a mismatched compressor the influence of downstream stable stage limits the extent of stall cells. Therefore, there is a possibility that the first stage of our geometry would become unstable before the second one. We wanted to determine if this was the case here. Running two axisymetric calculations on the two stages, we could compare the mass flow for the peaks of the pressure rise characteristics. The first stage included the first rotor and the first stator whereas the second stage was defined by the first stator followed by the second

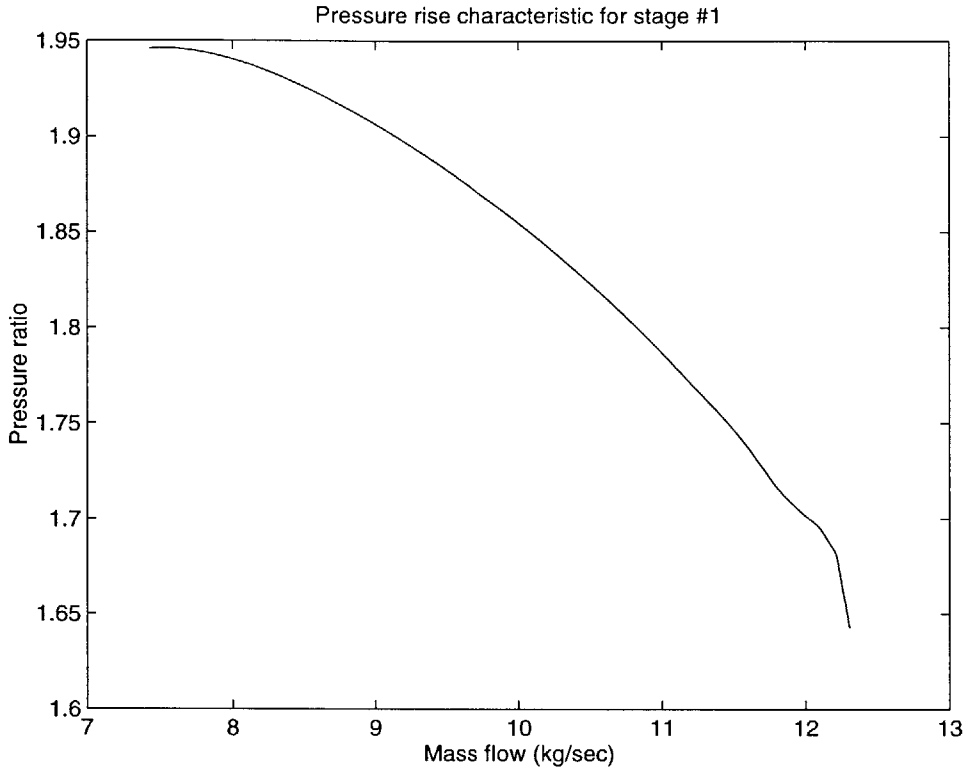

Figure 3-3: Pressure rise characteristic for the first stage.

rotor and the second stator.

Since the mass flow at the peak of the pressure rise characteristic of the first stage is higher than that of the second stage, the first stage tends to stall earlier than the second one. Therefore it is the most unstable stage of the compressor. It is deduced from this observation that the focus of the effort should be on the first stage stability behavior.

3.4 summary

For the two stage high speed compressor, the first stage appears to be more unstable than the second stage. In the next chapter, the stability behavior of the first rotor will be examined using an unsteady 3D flow solver to determine the role of the rotor tip clearance flow on setting compressor stability.

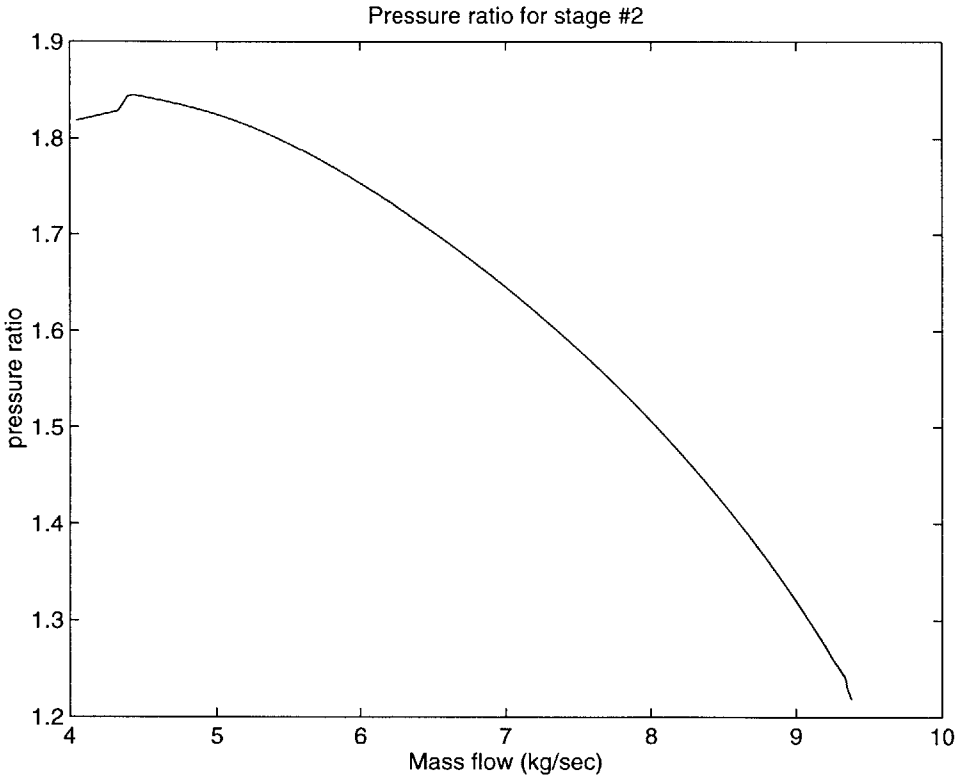

Figure 3-4: Pressure rise characteristic for the first stage.

CHAPTER 4

3D SIMULATIONS AND TIP LEAKAGE VORTEX INFLUENCE ON STABILITY

4.1 Introduction

The 2D calculations presented in chapter 2 show the flow behavior under the assumption of strip theory. We could calculate the pressure rise characteristic and determine the conditions under which a particular blade row would stall at a given spanwise position of each blade. We would like to be able to analyze the behavior of one complete row using the 3D version of Donald Hoying's solver: RS3. The contributions of such calculations are to better understand the mechanism involved in the tip region at the inception of the rotating stall. The effects inside this region are associated with three-dimensional flow and thus require the use of a 3D viscous flow solver. Under the condition for which the results of chapter 3 were obtained, the first stage would be more unstable relative to the second stage. As such, we will apply the solver for simulating flow in the first rotor of 2-stage high-speed compressor.

4.2 The 3D solver RS3

4.2.1 Solver equations

The solver implements the three-dimensional Navier-Stokes equations in rotational cylindrical coordinates

$$\vec{U} = \begin{pmatrix} \rho \\ \rho w_x \\ \rho w_\theta \\ \rho w_r \\ E'_t \end{pmatrix} \tag{4.1}$$

$$\vec{E} = \begin{pmatrix} \rho w_x \\ \rho w_x^2 + p - \Gamma_{11} \\ \rho w_x w_\theta - \Gamma_{12} \\ \rho w_x w_r - \Gamma_{13} \\ E'_t w_x + p w_x - q_x - \Gamma_{11} w_x - \Gamma_{12} w_\theta - \Gamma_{13} w_r \end{pmatrix} \tag{4.2}$$

$$\vec{F} = \begin{pmatrix} \rho w_\theta \\ \rho w_x w_\theta - \Gamma_{12} \\ \rho w_\theta^2 + p - \Gamma_{22} \\ \rho w_\theta w_r - \Gamma_{23} \\ E'_t w_\theta + p w_\theta - q_\theta - \Gamma_{12} w_x - \Gamma_{22} w_\theta - \Gamma_{23} w_r \end{pmatrix} \tag{4.3}$$

$$\vec{G} = \begin{pmatrix} \rho w_r \\ \rho w_x w_r - \Gamma_{13} \\ \rho w_\theta w_r - \Gamma_{23} \\ \rho w_r^2 + p - \Gamma_{33} \\ E_t' w_r + p w_r - q_r - \Gamma_{13} w_x - \Gamma_{23} w_\theta - \Gamma_{33} w_r \end{pmatrix} \tag{4.4}$$

$$\vec{S} = \begin{pmatrix} 0 \\ 0 \\ -\rho w_\theta w_r + 2\Omega r \rho w_r + \Gamma_{23} \\ \rho w_\theta^2 + p - 2\Omega r \rho w_\theta + \Omega^2 r^2 \rho - \Gamma_{22} \\ \Omega^2 r^2 \rho w_r \end{pmatrix} \tag{4.5}$$

Closure is obtained using the following relations,

$$E_t' = \rho \left(e + \frac{w_x^2 + w_\theta^2 + w_r^2}{2} \right) \tag{4.6}$$

$$q_x = k \frac{\partial T}{\partial x} \quad q_\theta = \frac{k}{r} \frac{\partial T}{\partial \theta} \quad q_r = k \frac{\partial T}{\partial r} \tag{4.7}$$

$$T = \frac{(\gamma - 1)\, e}{R} \tag{4.8}$$

$$p = (\gamma - 1)\, \rho e \tag{4.9}$$

where k, γ, and R are fluid dynamic constants.

4.2.2 Grid construction

The three-dimensional grid consists of stacking the two-dimensional O and H grid similar to those used for RS2. One change has been made from the original method though. Originally the O grids for hub to tip were first calculated and each intermediate O-grid

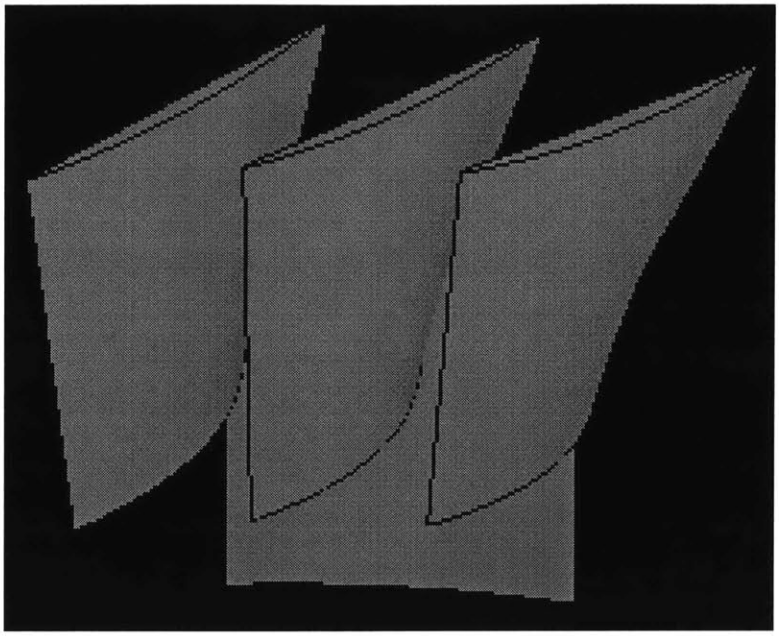

Figure 4-1: Rotor geometry for the 3D calculations.

was calculated with a linear interpolation of these. Since the blade geometry has a strong spanwise variation, the grid generation method has been modified accordingly to deal with the present geometrical configuration. Figure 4-1 shows the geometry used for the first 3D calculations.

4.2.3 Choice of blade number

An important choice that has to be made is the number of blades. It is indeed not possible to simulate the entire row of blades as the computational resources needed would be enormous. This is the reason why we need to choose a lower number of blades according to some constraints. We need to know if the row is going to stall either by modes or by 'spikes' . Therefore, we need to be able to capture the harmonics of the modal type stall. If we wanted to capture the first harmonic, we would need to simulate the whole row; thus we chose to use Longley criterion [15] that requires a computational domain with 11 blades if we want to capture the 6th harmonic of the modal type of stall inception. Fig 4-2 shows such a computational domain.

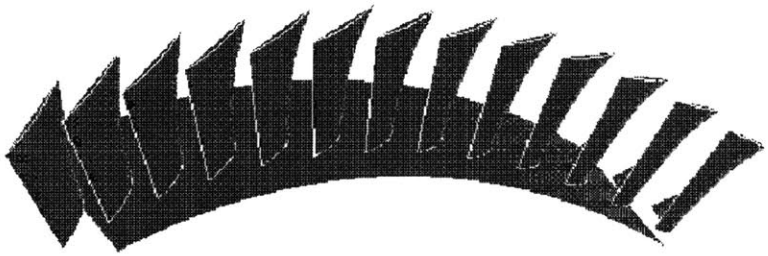

Figure 4-2: Computational domain with 11 blades.

4.2.4 Protocol of implementing the computational Experiments

The goal of these calculations is to have the rotor row operating at or near stall so that the inception and the development of instabilities can be studied. For this, we need to know where the instability point of the row stands. Since we cannot afford to determine this instability point by carrying out a calculation with 11 blades because of a huge computational time needed, it has become necessary to implement a preliminary set of calculations to determine what throttle position would trigger the instability. In a manner similar to the 2D calculation, the throttle is set to 1.0 at the beginning of the calculation until it reaches a steady state. Then it is possible to change the throttle by discrete decrement and each time we must get a steady state. Fig 4-3 shows the average mass flow going through the system every 10 iterations. It gives us a good idea of the convergence of the calculations.

We want to determine the impact of tip leakage vortices on the inception of stall. According to Donald Hoying's hypothesis, tip leakage vortices going forward of the blade passage can trigger rotating stall. However, this hypothesis has been questionned by Duc Vo and the phenomenon needs to be further studied to determine the manner for which tip clearance flow triggers compressor stall. The goal of this first set of calculations is to calculate a steady state of the flow for which the tip leakage vortex is lined up with the leading edges of the blades.

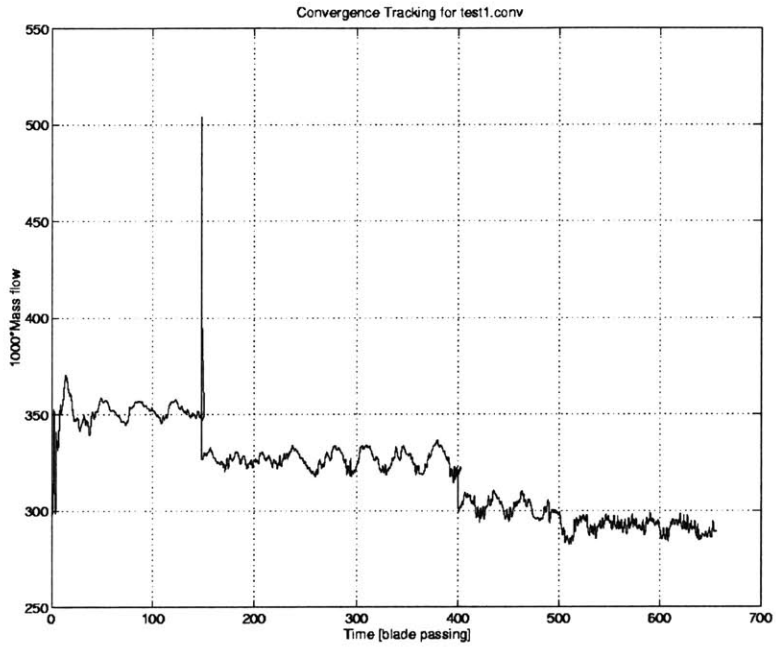

Figure 4-3: Mass flow convergence for 1 blade passage.

4.3 Single blade passage calculations

This first set of calculations consists of single blade passage calculations for determining the conditions when the rotor is operating near stall. These conditions are then adopted for use in the 11 blade passage simulation.

4.3.1 Before stall

First, we need to obtain a steady state flow situation prior to compressor stalling. With a throttle open to 65 % of the maximum throttle setting, we can see on figure 4-4 that the flow vectors are not showing a separation on the suction side of the blades. There is a region of low mach number on the suction side of the blade passage but the flow is still attached and therefore we can say that the mid span region is unstalled for a throttle setting equal to 65% of the exhaust surface.

The computed results of Figure 4-5 is a contour on a r-θ plane at 95% of the blade span. The vorticity contour shows the path of the tip leakage vortices. which for this case are dowstream of the leading edge plane. It can be noticed that the impact of these vortices on the suction side of the next blade are located downstream of the leading edge. According

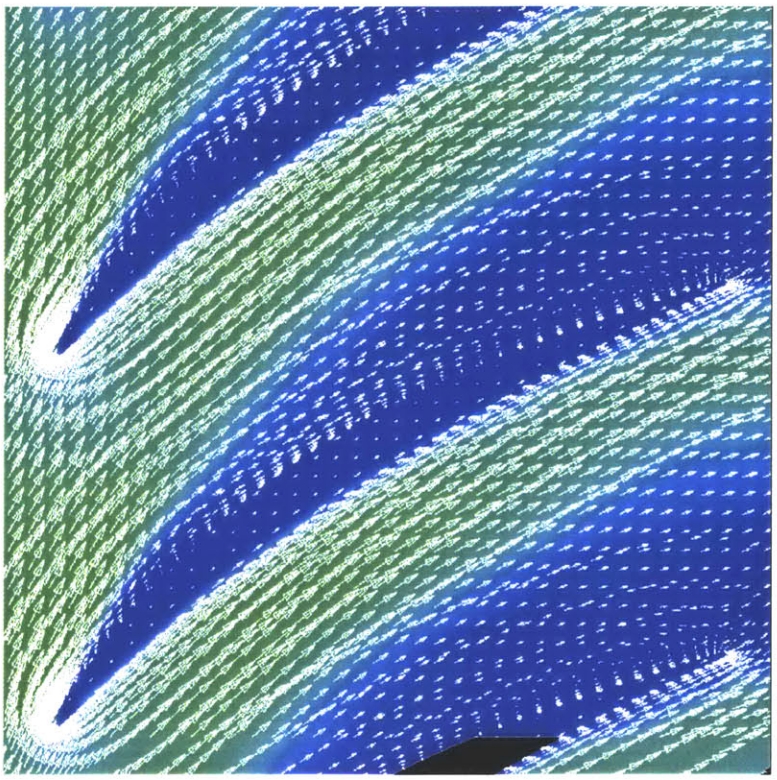

Figure 4-4: Mach number and flow vectors at mid-span for a throttle setting at 0.65

to Donald Hoying hypothesis, this fact indicates that the blade row is on the stable portion of the pressure rise characteristic. Therefore we can further reduce the throttle to reach the peak of this characteristic.

4.3.2 Critical point

For a throttle set to 57% of the maximum throttle setting, Figure 4-6 shows the Mach number distribution on an r-θ plane at 95% of the span of the rotor. We can clearly see that there is a well-defined limiting line going from one leading edge to another. This separates the upstream clean flow from the flow between the blades that include tip clearance flow.

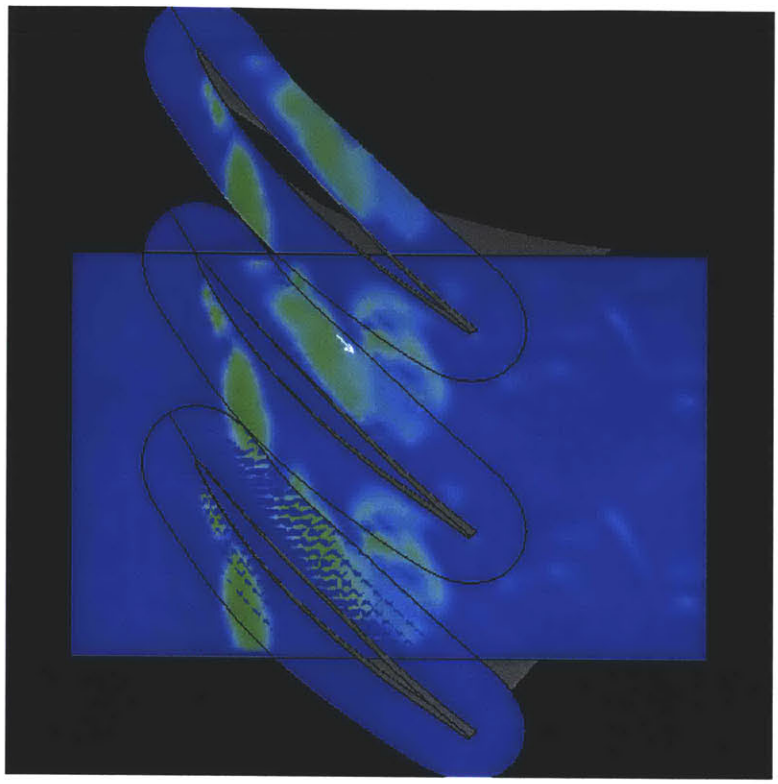

Figure 4-5: Vorticity plot at 95% of the span for a throttle setting at 0.65

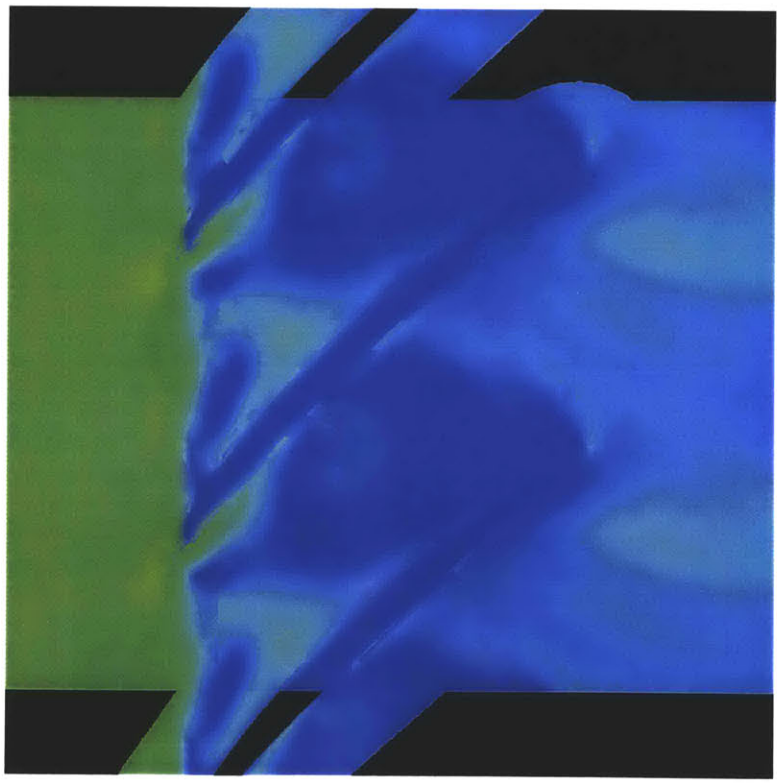

Figure 4-6: Mach number contour at 95% span in a r-θ plane for a throttle setting at 0.57

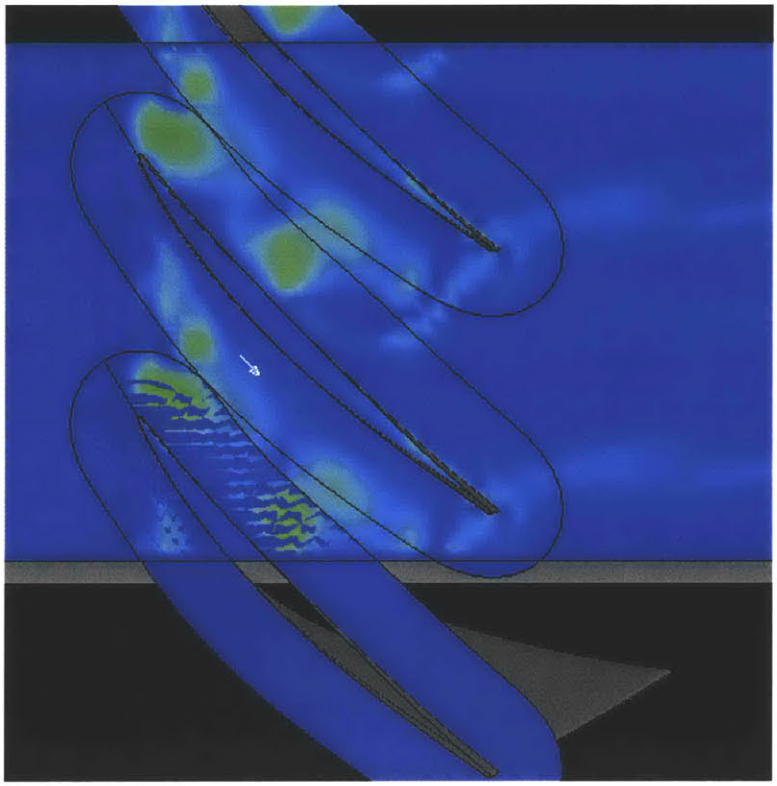

Figure 4-7: Vorticity plot at 95% of the span for a throttle setting at 0.57

4.4 The multi-blade passages calculations

4.4.1 Steady state problem

The preceding calculation allowed us to determine the throttle position for the potential inception of flow instabilities. We can now proceed with the 11 blade passage calculations to determine the conditions for which the rotor would stall.

We first set the calculation to reach a steady-state with a throttle fully-opened before we reduce it to a setting corresponding to the instability point. Using the available computational resources at MIT Gas Turbine Laboratory, it took four weeks to reach a steady-state point.

Figure 4-8 shows the static pressure contour on a mid-span plane. We notice that the static pressure is lower at the exit of the rotor than at its inlet. We must analyse the flow to determine the cause of such a static pressure drop. Figure 4-9 shows the velocity vectors at the leading edge of a rotor blade. We notice a separation bubble on the pressure side of

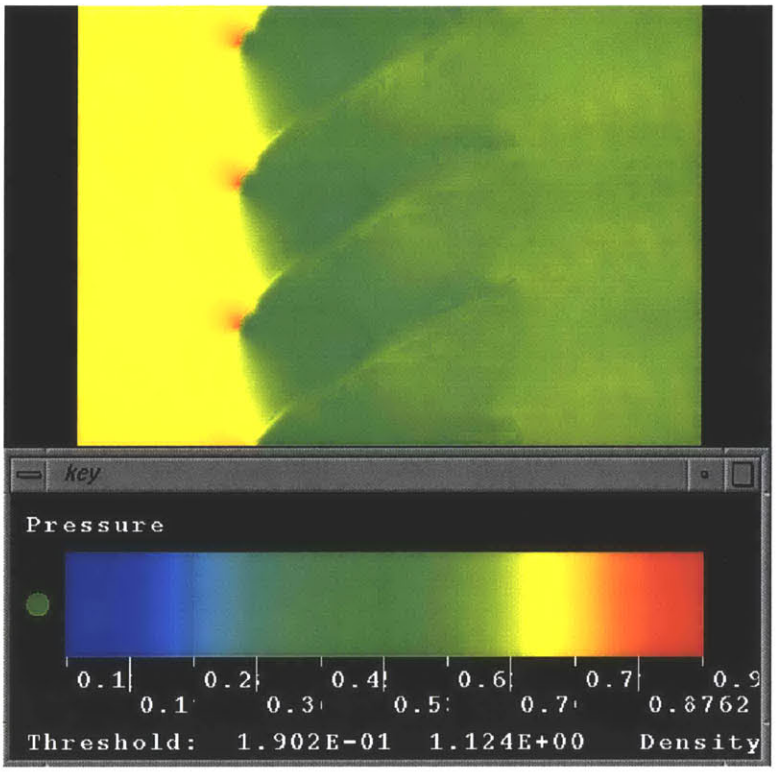

Figure 4-8: Pressure plot for a cut at mid-span.

the rotor blade. This bubble creates a high blockage at the inlet of the blade passage. This could be the cause of the static pressure decrease.

4.4.2 problem analysis

To understand what is the cause of the negative angle of incidence on the leading eadge of the rotor blade, we checked the differences between the 1 blade passage and the 11 blade passage calculations. Beside the number of blade, we kept the same boundary conditions, the same rotational speed of the rotor and the same inlet pressure and inlet incidence angles.

To be able to do a calculation on a large grid representing 11 blade passage, it was necessary to reduce the number of grid points in the azimuthal direction thus changing the grid aspect ratio. This could have been a reason for the change in the computed flow behavior between the two calculations.

To check this assumption, we have decided to run another 1 blade passage calculation with the same grid characteristics as that used in the 11 blade passage. Figure 4-10 shows

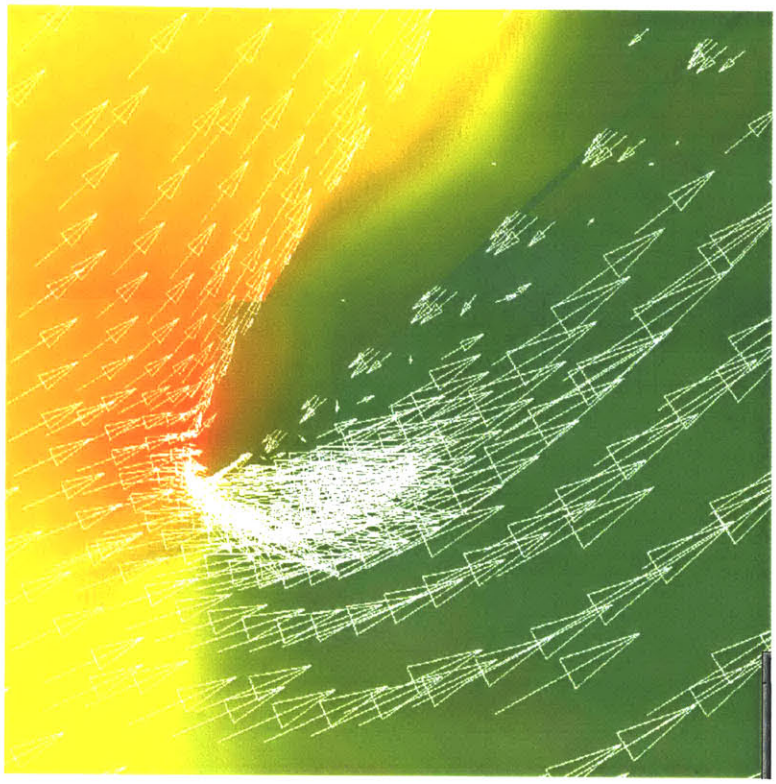

Figure 4-9: Velocity vector at the leading edge of the rotor for a cut at mid-span.

that the same phenomenon appear at the leading edge as a transient. Figure 4-11 shows the leading edge flow at a later time and we can notice that the bubble has disappeared. This phenomenon was not present for the first one blade passage calculation. Therefore this study implies that grid resolution and the aspect ratio of the cells can have an influence on the solution behavior as it approaches the equilibrium state.

4.4.3 Summary

In this chapter, we implemented a 1-blade-passage calculation to estimate the right throttle position to be set for the following 11-blade-passage calculation. Having found a value of 0.57, we could run the next calculation but the negative flow angle at the leading edge of the rotor created a high blockage region and we had to stop the calculation. Running another 1-blade-passage calculation, we found that the grid density and aspect ratio had an impact on the results of the calculations obtained using Hoying's code. The lack of additional computational resources put a constraint on the completion of the 11-blade passage calculation for delineating the fluid dynamic process that set the compressor stall.

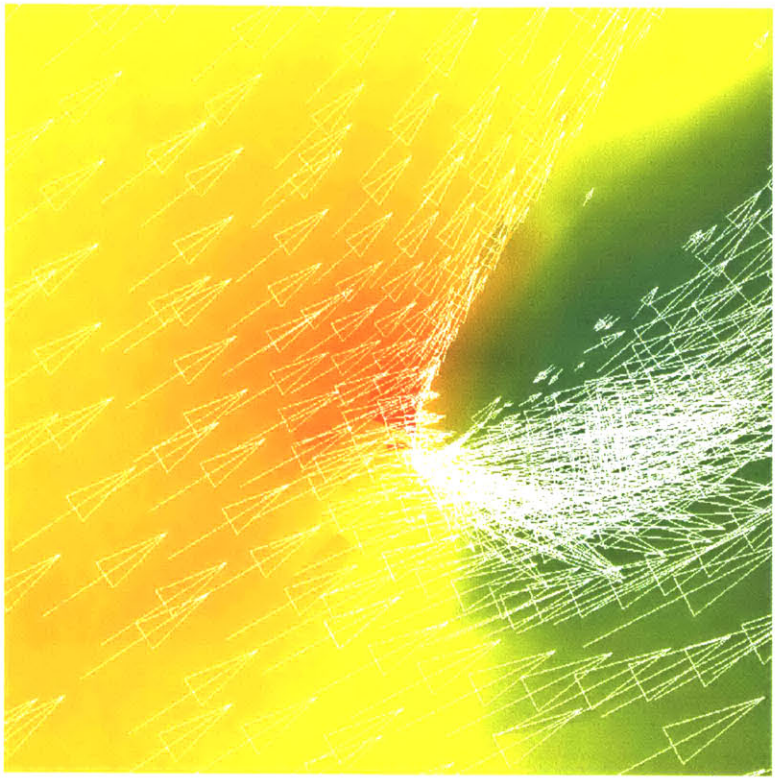

Figure 4-10: Velocity vector during transient

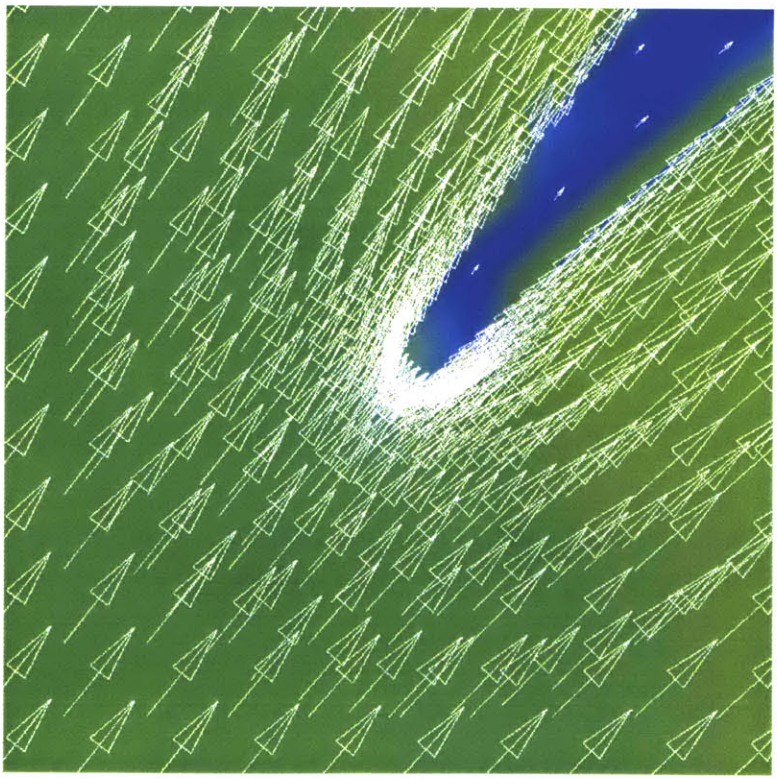

Figure 4-11: Velocity vector after transient

CHAPTER 5

CONCLUSIONS

The goal of this study is to demonstrate the feasibility of implementing a complete stability analysis within the design loop of a multistage compressor. To accomplish this, two computational models developed in the Gas Turbine Laboratory have been used. The first one, developed by Yifang Gong, is a row-by-row body force representation that allows the stability behavior of a multi-stage compressor to be analyzed. The second model was developed by Donald Hoying. It computes the 3-D features of the flow in a multi-blade passage of an isolated blade row. The approach would consist of first implementing a 3-D or a set of 2-D calculations for each of the blade row to establish the row-by-row body force representation of a multi-stage compressor. The latter is then used to determine the most unstable stage. Finally a multi-blade passage calculation is carried out for the rotor of the most unstable stage with the objective of determining the flow event responsible for setting compressor stall.

5.1 Summary and conclusions

An attempt was made to assess the feasability of implementing a multi-stage compressor stability analysis during the course of its design. This involves the application of two computational methodology : (1) Gong's computational model which consists of a blade-row-by-blade-row representation of a compressor for stability analysis, (2) Hoying's 3-D flow solver for implementing single blade passage calculation as well as multi-blade passage calculation. The original plan was to use the single blade-passage calculation from (2) to

establish the blade-row-by-blade-row body force representation of the compressor in (1) followed by its use to determine the most unstable stage. A multi-blade passage calculation was then to be implemented for the rotor of the most unstable stage to determine the conditions that set the compressor stability. The computed results were then to be used to redesign the compressor to improve its stability behavior. However only a subset of the calculations of the originally proposed calculations have been implemented due to constraints imposed by time and the available computational resources. These are: (i) A set a 2-D single blade passage calculations at discrete spanwise locations for each of the four blade rows. (ii) Use of Gong's methodology to determine the most unstable stage based on axisymmetric calculations. (iii) Use of Hoying's code to implement a set of single blade passage calculations and one 11-blade passage calculations. The 3-D 11-blade passage calculations was implemented to determine the role of tip leakage vortex in setting the compressor stability. This was based on Hoying's hypothesis which has since be called into question by Duc Vo [27].

(i) and (ii) brought us the conclusion that the first stage was the most unstable and that was the reason why we focused our efforts on this stage in (iii). During the course of implementing (iii), we discovered the impact of the grid resolution and the cells aspect ratio on the the outcome of the calculations. The comparison made between two calculations with identical boundary and initial conditions but different grids raised the issue of the sensitivity of the computed results based on the selected grid resolution and distribution.

BIBLIOGRAPHY

[1] Camp, T. R. "Aspects of The Off-Design Performance of Axial Flow Compressors," Ph.D. Dissertation, University of Cambridge (1995)

[2] Camp, T. R. and Day, I. J. "A Study of Spike and Modal Stall Phenomena in a Low-Speed Axial Compressor," ASME paper No. 97-GT-526 (1997)

[3] CHIENG, C. C. AND LAUNDER, B. E. "On the Calculation of Turbulent Heat Transport Downstream from an Abrupt Pipe Expansion". *Numerical Heat Transfer*, Vol. 3, 1980, pp.189-207.

[4] Chue, R., Hynes, T. P., Greitzer, E. M., and Tan, C. S. "Calculations of Inlet Distortion Induced Compressor Flow Field Instability," *International Journal of Heat and Fluid Flow*, Vol. 10 (1989), pp.211-223

[5] Cumpsty, N. A., and Greitzer, E. M. "A Simple Model for Compressor Stall Cell Propagation," *ASME Journal of Engineering for Power* Vol.104 (1982), pp.170-176

[6] Day, I. J. "Stall Inception in Axial Flow Compressors," *ASME Journal of Turbomachinery* Vol. 115 (1993), pp.1-9

[7] Dunham, J. "Non-Axisymmetric Flows in Axial Compressors" *mechanical Engineering Science* Monograph No. 3 (1965)

[8] Emmons, H. W., Pearson, C. E., and Grant, H. P. "Compressor Surge and Stall Propagation" *Transactions of The ASME* Vol.79 (1955), pp.455-469

[9] Greitzer, E. M., "The Stability of Pumping System — The 1980 Freeman Scholar Lecture," *ASME Journal of Fluids Engineering*, Vol. 103 (1981), pp.193-242

[10] GILES, M. B. "Non-Reflecting Boundary Conditions for the Euler Equations". CFDL-TR-88-1, Computational Fluid Dynamics Laboratory, Massachusetts Institute of Technology, February 1988.

[11] GONG, Y. "A Computational Model For Rotating Stall and Inlet Distortions in Multistage Compressors". PhD. Thesis, Massachusetts Institute of Technology, Department of Aeronautics and Astronautics, September 1996.

[12] HOYING, D. A. "Blade passage Flow Structure Effects On Axial Compressor Rotating Stall Inception ". PhD. Thesis, Massachusetts Institute of Technology, Department of Aeronautics and Astronautics, September 1996.

[13] Hoying, D. A., Tan, C. S., Vo, H. D., and Greitzer, E. M. "Role of Blade Passage Flow Structures in Axial Compressor Rotating Stall Inception," ASME paper 98-GT-588 (1998)

[14] LAUNDER, B. E. AND SPALDING, D. B. *Computer Methods in Applied Mechanics and Engineering.* Vol. 3. 1974. pp. 269–289.

[15] Longley, J. P. "A Review of Non-Steady Flow Models for Compressor Stability," ASME paper 93-GT-17 (1993)

[16] Longley, J. P., Shin, H. W., Plumley, R. E., Silkowski, P. D., Day, I. J., Greitzer, E. M., Tan, C. S., and Wisler, D. C., "Effects of Rotating Inlet Distortion on MultiStage Compressor Stability," *ASME Journal of Turbomachinery*, Vol. 118 (1996), pp.181-188

[17] Longley, J. P., "Calculating the Flowfield Behaviour of High-Speed Multi-Stage Compressors," ASME paper No. 97-GT-468 (1997)

[18] Marble, F. E., 1964 "Three-Dimensional Flow in Turbomachines," *Aerodynamics of Turbines and Compressors, Vol. X of High Speed Aerodynamics and Jet Propulsion*, Hawthorne, W. R., ed. Princeton University Press, Princeton, NJ., pp.83-166

[19] Moore, F. K. and Greitzer, E. M., "A Theory of Post-Stall Transients in Axial Compression Systems: Part I,II," *ASME Journal of Engineering for Gas Turbines and Power*, Vol. 108 (1986), pp. 68-76, pp. 231-239

[20] Paduano, J. D., and Gysling, D. L. "Rotating Stall in Axial Compressors: Nonlinear Modeling for Control," SIAM Conference on Control and its Applications, Minneapolis, (1992)

[21] Reid, C. "The Response of Axial Flow Compressors to Intake Flow Distortion," ASME paper 69-GT-29 (1969)

[22] Seitz, P. Private Communications via Vo, (1999)

[23] Silkowski, P. D., "Measurements of Rotor Stalling in a Matched and a Mismatched Multistage Compressor," GTL Report No. 221 (1995), Gas Turbine Laboratory, Massachusetts Institute of Technology

[24] STEGER, J. L. AND SORENSON, R. L. "Automatic Mesh-Point Clustering Near a Boundary in Grid Generation with Elliptic Partial Differential Equations". *Journal of Computational Physics*, Vol. 33, 1979, pp.405-410.

[25] TAM, C. K. W. AND WEBB J. C. "Dispersion-Relation-Preserving Finite Difference Schemes for Computational Acoustics". *Journal of Computational Physics*,Vol. 107, 1993, pp.262-281.

[26] Van Zante, D., Strazisar, A., Wood, J., Hathaway, M. and Okiishi, T. "Recommendations for Achieving Accurate Numerical Simulation of Tip Clearance Flows in Transonic Rotors" ASME paper 99-GT-390 (1999)

[27] Vo H. D., Private Communications, (1999)

APPENDIX A

BODY FORCE MODEL COEFFICIENTS

At the time this thesis is written, the research compressor of this study has not been built yet. This is the reason why we have but little information about its behavior. However, the axisymetric calculations, already done on it, have led to an estimation of a portion of each row's pressure rise characteristic and efficiency. Since the coefficients of Gong's model have been calibrated with the data of Rotor 35 from GE. It has been necessary to conduct a parameter analysis of the coefficients in order to adapt the model to our case. The criterion chosen here is maximum static pressure ratio reached by the pressure rise characteristic. The original coefficients used by Yfong Gong are

$$K_n = 4.2 - 3.3 * \alpha$$

$$K_p = 0.04$$

Coefficient K_p governs the viscous influence on the flow. The first idea is to analyze its influence on the pressure rise characteristic shown on figure A-1.

Coefficient K_n governs the amount of flow turning due deviation angle between the local direction of the flow and the local metal angle. Multiplying this coefficient by the variable λ allows us to understand the influence of this parameter on the pressure rise characteristic of the row (Fig. A-2).

Comparing these parametric studies to previous calculations led us to choose a new set of coefficients, which have been implemented in the model. They are:

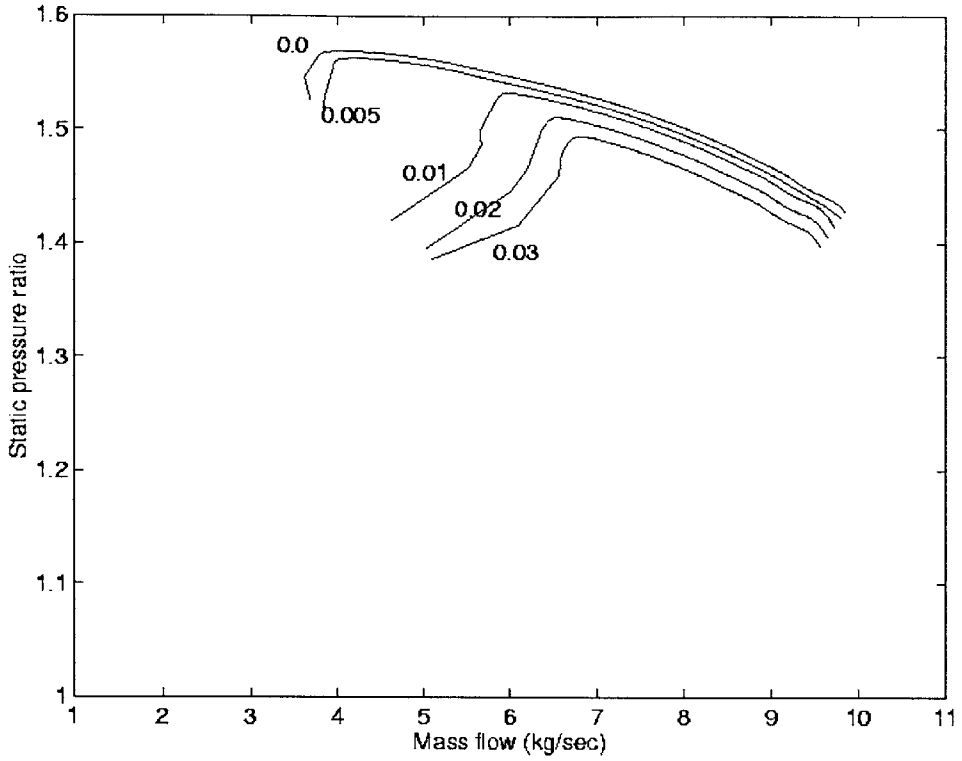

Figure A-1: Comparison of pressure rise characteristic for different values of K_p.

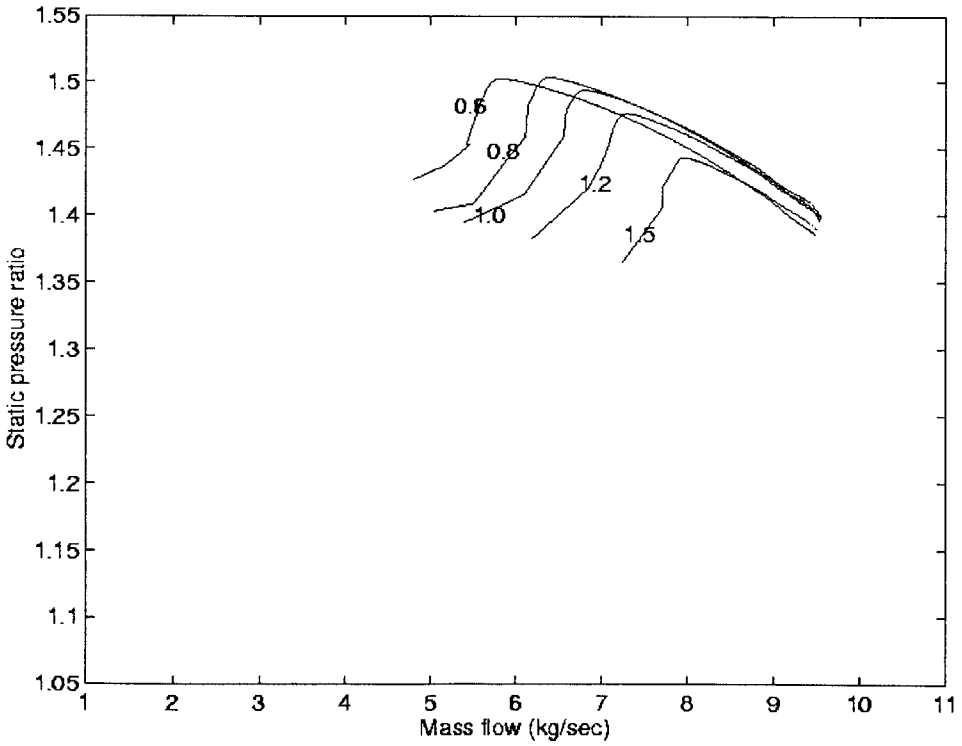

Figure A-2: Comparison of pressure rise characteristic for different values of K_n.

$$K_n = 0.8 * (4.2 - 3.3 * \alpha)$$

$$K_p = 0.005$$